Mathematics

https://www.aimspress.com/journal/Math

AIMS Mathematics, 11(4): 10611–10637.
DOI:10.3934/math.2026437
Received: 15 February 2026
Revised: 22 March 2026
Accepted: 27 March 2026
Published: 17 April 2026

Research article

Localized wave solutions of the second-order Alice-Bob Benjamin-Ono equation via KP-hierarchy reduction

Majid Madadi[1,2] **and Lanre Akinyemi**[3,*]

[1] Department of Mathematics, Saveetha School of Engineering, Saveetha Institute of Medical and Technical Sciences, Saveetha University, Chennai 602105, Tamil Nadu, India
[2] Research Center of Applied Mathematics, Khazar University, Baku, Azerbaijan
[3] Department of Mathematics, Prairie View A&M University, Texas, USA

* **Correspondence:** Email: Laakinyemi@pvamu.edu.

Abstract: Alice-Bob systems offer a powerful framework for describing nonlocal correlations between spatially separated physical events. In this paper, we investigate nonlinear wave structures of the second-order Alice-Bob Benjamin-Ono system, an integrable nonlocal model for two-place correlated phenomena. Using the Kadomtsev-Petviashvili hierarchy reduction method, we derive explicit Gram-determinant breather solutions and construct higher-order breather and breather-soliton interactions. By combining block-determinant formulations with long-wave limits, we obtain semi-rational solutions that describe interactions among breathers, solitons, and lump waves. In addition, through bilinear theory and Schur polynomial techniques, we derive general higher-order rogue wave solutions in compact determinant form. These solutions exhibit rich geometric patterns, including triangular and polygonal rogue wave configurations, whose orientations are controlled by free complex parameters while preserving peak amplitudes. The results reveal diverse interaction dynamics and complex localized wave structures in the second-order system. This unified determinant framework significantly enriches the family of exact solutions and provides new insights into nonlinear wave dynamics in nonlocal integrable systems.

Keywords: Alice-Bob systems; Benjamin-Ono equation; Kadomtsev-Petviashvili-hierarchy reduction; rational solutions; rogue wave
Mathematics Subject Classification: 35Q51, 37K10, 37K40

---

1. Introduction

In nature, many physical events occurring at different locations and different times are not independent; instead, they are closely correlated or even entangled. Large-scale climate phenomena provide striking examples: Variations in Arctic sea ice can influence extreme weather in distant regions [1, 2], and long-period ocean-atmosphere interactions can trigger abnormal rainfall or drought thousands of kilometers away [3]. In astrophysics, the detection of gravitational waves has been linked to black hole mergers that occurred billions of light-years from Earth [4]. In quantum mechanics, measurements performed on one particle may instantaneously affect the state of another spatially separated particle [5]. Even in secure communications, information sent by "Alice" can only be decoded by "Bob" through a specific key that correlates the two sides [6].

Despite these ubiquitous long-range correlations, most classical physical models are constructed locally, describing the evolution of a field around a single space-time point (x, t). Traditional nonlinear evolution equations, such as the Korteweg-de Vries (KdV), modified KdV (mKdV), nonlinear Schrödinger (NLS), sine-Gordon, and Kadomtsev-Petviashvili (KP) equations, are built on this locality principle. However, when two correlated or entangled events occur at different space-time points, local models may not be sufficient to capture the underlying mechanism. This observation motivates the search for new mathematical frameworks capable of describing intrinsically two-place physical phenomena.

A major step toward this direction was made when Ablowitz and Musslimani introduced integrable nonlocal nonlinear Schrödinger equations through parity-time (PT) symmetric reductions [7]. In these models, the field at position x is directly coupled with its complex conjugate evaluated at the reflected position $-x$. Their discovery demonstrated that nonlocality and integrability can coexist, triggering extensive research on nonlocal nonlinear systems, including nonlocal KdV [8], nonlocal mKdV [9], and nonlocal KP [10] equations.

Inspired by these developments, Lou proposed the concept of Alice-Bob (AB) systems, which provides a systematic way to describe two correlated events occurring at distinct space-time points [11, 12]. In this framework, the event at (x, t) is called the Alice event and is denoted by $A(x, t)$, while the correlated event at (x', t') is called the Bob event, denoted by $B(x', t')$. The two events are linked through a specific operator $\hat{f}$, such that

$$B = \hat{f}A.$$

For one-dimensional systems, the operator $\hat{f}$ typically involves a combination of shifted parity and delayed time-reversal transformations,

$$x' = -x + x_0, \quad t' = -t + t_0,$$

possibly accompanied by charge conjugation. Because the transformed point (x', t') is generally far from (x, t), the resulting AB systems are inherently nonlocal. The evolution at one location depends directly on the state of the system at another distant location.

An important feature of AB systems is that they naturally admit both symmetry-invariant and symmetry-breaking solutions. Some solutions remain invariant under the combined shifted parity and delayed time-reversal transformation. These correspond, in a sense, to symmetric correlations between the two events. More intriguingly, however, there also exist symmetry-breaking solutions, for which the transformation of a solution does not coincide with the solution itself. Such solutions lead to new types of wave phenomena, including nonlocal solitons, kink structures, rogue waves, and novel interaction behaviors that have no counterparts in purely local models.

Since their introduction, AB systems have been constructed for a variety of integrable equations. These studies reveal that nonlocal correlations can significantly enrich the dynamical structure of nonlinear wave equations, providing new perspectives on integrability, symmetry, and long-range interactions. Therefore, AB systems offer not only a mathematically appealing generalization of classical integrable models but also a conceptually meaningful framework for describing two-place correlated physical processes. Their study continues to deepen our understanding of nonlocal nonlinear dynamics and correlated wave phenomena.

The Benjamin-Ono (BO) equation is a nonlinear, integrable partial integro-differential equation that models one-dimensional internal waves in deep, stratified fluids. In contrast, the KdV equation is more appropriate for shallow-water dynamics. The standard BO equation is

$$u_t + H[u_{xx}] + uu_x = 0, \tag{1.1}$$

where $u(x,t)$ is a real-valued function and H denotes the Hilbert transform,

$$H[f](x) = \frac{1}{\pi}\,\text{P.V.}\int_{-\infty}^{\infty} \frac{f(y)}{x-y}\,dy, \tag{1.2}$$

with P.V. indicating the Cauchy principal value. The nonlinear advection term uu_x and the nonlocal dispersive effect introduced by the Hilbert transform together produce rich wave phenomena. The BO equation is completely integrable, possesses the Painlevé property, and admits soliton solutions which, unlike the exponentially decaying KdV solitons, decay algebraically. Foundational studies include [13–16].

Motivated by the need to capture higher-order nonlinear and dispersive effects, a second-order form of the BO equation was introduced in [17, 18]. The second-order (1+1)-dimensional integrable BO equation takes the form

$$u_{tt} + \alpha(u^2)_{xx} + \beta u_{xxxx} = 0, \tag{1.3}$$

where α and β are nonzero constants characterizing the strength of the nonlinearity and the effective depth-induced dispersion, respectively. Here, $u(x,t)$ represents the fluid surface displacement. Analogous in structure to the Boussinesq equation [19], this higher-order BO model combines weak quadratic nonlinearity with dispersive regularization. This second-order BO equation retains several key integrability features: It has the Painlevé property [20], admits N-soliton solutions [21], and supports reductions derived from conservation laws. Additional studies have established a hierarchy via Lenard recursion relations [22] and constructed explicit algebro-geometric solutions using theta functions [23]. Moreover, rogue wave, periodic breather, and lump-type solutions have been generated through methods including Hirota's bilinear approach, homoclinic/heteroclinic breather limits, homoclinic tests, and parameter perturbations, with their spatiotemporal dynamics examined through extreme value theory [24, 25].

In physical applications, the higher-order terms in the second-order BO equation become relevant when the weakly nonlinear and weakly dispersive assumptions of the classical BO model are no longer sufficient. In stratified fluids, the standard BO equation describes long internal waves propagating along a density interface in deep water. When the wave amplitude increases or strong density gradients are present, higher-order nonlinear corrections become important. In this regime, the term $\alpha(u^2)_{xx}$ represents enhanced quadratic nonlinearity associated with stronger wave steepening. The fourth-order dispersive term βu_{xxxx} accounts for higher-order dispersion that may arise when the wavelength becomes comparable to the thickness of the stratified layer. Similar corrections also appear in nonlinear optical media for ultrashort pulse propagation, where β corresponds to higher-order group-velocity dispersion. Thus, the second-order BO equation becomes relevant when moderate-amplitude internal waves or strongly dispersive media require corrections beyond the standard BO approximation.

In [26], the authors demonstrated that, based on the principle of the AB system, by introducing the transformation

$$u = \frac{1}{2}(A + B), \tag{1.4}$$

into Eq (1.3), one can derive the corresponding nonlocal AB-BO system in the form

$$A_{tt} + B_{tt} + \alpha(A_x + B_x)^2 + \alpha(A + B)(A_{xx} + B_{xx}) + \beta(A_{xxxx} + B_{xxxx}) = 0. \tag{1.5}$$

Furthermore, Eq (1.5) can be decomposed into the following coupled system:

$$\begin{aligned} A_{tt} + \frac{\alpha}{2}(A_x + B_x)(3A_x - B_x) + \frac{\alpha}{2}(3A + B)A_{xx} + \frac{\alpha}{2}(A - B)B_{xx} + \beta A_{xxxx} &= 0, \\ B_{tt} - \frac{\alpha}{2}(A_x + B_x)(A_x - 3B_x) + \frac{\alpha}{2}(A + 3B)B_{xx} - \frac{\alpha}{2}(A - B)A_{xx} + \beta B_{xxxx} &= 0. \end{aligned} \tag{1.6}$$

It is evident that systems (1.6) are integrable and support a Lax pair. In addition, symmetry-breaking soliton, breather, and lump solutions for these systems have been derived using the Hirota bilinear form [26].

By applying the logarithmic transformations

$$\begin{aligned} A &= \frac{6\beta}{\alpha}[\ln \mathfrak{g}]_{xx} + \zeta_1[\ln \mathfrak{g}]_{xxx} + \zeta_2[\ln \mathfrak{g}]_{xxt} + u_0, \\ B &= \frac{6\beta}{\alpha}[\ln \mathfrak{g}]_{xx} - \zeta_1[\ln \mathfrak{g}]_{xxx} - \zeta_2[\ln \mathfrak{g}]_{xxt} + u_0, \end{aligned} \tag{1.7}$$

the AB-BO system (1.6) is converted into the following bilinear equation:

$$[\beta D_x^4 + 2u_0\alpha D_x^2 + D_t^2]\mathfrak{g}.\mathfrak{g} = 0, \tag{1.8}$$

where ζ_1 and ζ_2 are arbitrary constants, u_0 is an arbitrary constant seed solution, and $\mathfrak{g} = \mathfrak{g}(x, t)$ is a real-valued function of the independent variables x and t. Here, D_x^4, D_x^2, and D_t^2 denote Hirota's bilinear differential operators.

It is useful to note that, in order to obtain the bilinear equation using the Bell polynomial approach [27], we proceed as follows. First, we substitute the following expressions into the main AB-BO system (1.6):

$$A = u_0 + \frac{6\beta}{\alpha}q_{xx} + \zeta_1 q_{xxx} + \zeta_2 q_{xxt}, \quad B = u_0 + \frac{6\beta}{\alpha}q_{xx} - \zeta_1 q_{xxx} - \zeta_2 q_{xxt}, \tag{1.9}$$

where $q = q(x, t)$. Adding the resulting equations yields the following:

$$\frac{12\beta}{\alpha}(12\beta\, q_{xxxx}q_{xx} + 12\beta\, q_{xxx}^2 + \beta\, q_{xxxxxx} + 2\alpha u_0 q_{xxxx} + q_{xxtt}) = 0. \tag{1.10}$$

Integrating twice with respect to x (while ignoring the integration constants) gives

$$\beta\left(q_{xxxx} + 6q_{xx}^2\right) + 2\alpha u_0 q_{xx} + q_{tt} = 0. \tag{1.11}$$

The above equation can be written in terms of the P-polynomials as

$$\beta P_{4x}(q) + 2\alpha u_0 P_{2x}(q) + P_{2t}(q) = 0. \tag{1.12}$$

This equation is equivalent to the bilinear form in Eq (1.8) when the dependent variable transformation $q = \ln(\mathfrak{g})$ is considered. When $\zeta_1 = \zeta_2 = 0$, Eq (1.8) reduces to the standard Cole-Hopf-type transformation associated with the classical BO Eq (1.1). Exact wave solutions reveal the rich dynamics of nonlinear systems. Solitons are localized waves that maintain their shape; breathers are oscillatory, localized structures; and rogue waves are large, transient waves that appear unpredictably. Analytical methods such as Hirota's bilinear method [28], Wronskian approach [29], Darboux transformations [30], inverse scattering [31], modify $\left(\frac{G'}{G}\right)$-expansion method [32], improved Sardar sub-equation method [33], and KP-reduction [34] provide systematic tools to construct these solutions for integrable systems.

In this paper, we develop a systematic and unified framework for constructing exact determinant-type solutions to the second-order AB-BO system (1.6). By employing a KP-hierarchy reduction approach, we derive explicit breather solutions in Gram-determinant form and further extend the construction to semi-rational solutions describing interactions between breathers, solitons, and lumps. Moreover, by combining bilinear techniques with Schur polynomial expansions, we obtain general higher-order rogue wave solutions and analyze their dynamical structures, including asymmetric deformations induced by higher-order dispersive parameters. Compared with previous studies, our work provides the first comprehensive treatment of breather, semi-rational, and higher-order rogue wave solutions for the second-order AB-BO equation within a unified determinant framework, revealing rich multi-structure interactions and novel geometric patterns such as triangular and polygonal rogue wave configurations. These results significantly enrich the solution space and deepen the understanding of nonlocal integrable dynamics in AB systems.

The remainder of this paper is organized as follows. In Section 2, we employ the KP-hierarchy reduction method to derive determinant representations of breather-type solutions for the second-order AB-BO system (1.6). Moreover, the section is devoted to the construction of semi-rational solutions, describing the interactions between breathers, solitons, and lump waves through a block-determinant formulation and long-wave limit procedures. In Section 3, by means of Schur polynomial techniques and bilinear theory, we obtain general higher-order rogue wave solutions and investigate their spatiotemporal structures, including the formation of multi-peak and polygonal rogue wave patterns. Finally, we summarize the main results in Section 4.

2. Determinant-based solutions

In this part, we construct breather wave solutions in determinant form for the AB-BO system (1.6) using a reduction procedure associated with the KP hierarchy. This methodology, originally introduced by the Kyoto School [35, 36], has proven to be an effective framework for producing exact soliton-type solutions of nonlinear partial differential equations. The central concept behind the KP hierarchy reduction is to interpret the bilinear representation of the target equation as a constrained member of the broader KP hierarchy. Based on this viewpoint, one introduces a tau function that satisfies the bilinear equations within the KP hierarchy [40], which is defined as

$$\tau_n = \det_{1\le i,j\le N}\Big[\delta_{i,j} + \frac{p_i+q_j}{p_i+q_j}\exp(\Phi_i+\Psi_j)\Big], \tag{2.1}$$

with

$$\Phi_i = p_i z_1 + p_i^2 z_2 + p_i^3 z_3 + \Phi_{i,0}, \quad \Psi_j = q_j z_1 - q_j^2 z_2 + q_j^3 z_3 + \Psi_{j,0}. \tag{2.2}$$

In this expression, p_i, q_j, $\Phi_{i,0}$, and $\Psi_{j,0}$ denote arbitrary complex parameters, $\delta_{i,j}$ represents the Kronecker delta, and z_i are independent variables. The tau function defined above is known to satisfy a sequence of bilinear relations belonging to the KP hierarchy, one of which is as follows:

$$\Big[D_{z_1}^4 + 3D_{z_2}^2 - 4D_{z_1}D_{z_3}\Big]\tau_n\cdot\tau_n = 0. \tag{2.3}$$

To derive the determinant expression of the tau function, we briefly recall a standard construction from the KP hierarchy. In the KP framework, solutions of the bilinear equations can be generated from a set of exponential wave functions that satisfy the linear dispersion relations associated with the hierarchy. Let ϕ_i and ψ_j denote such eigenfunctions, which can be written in exponential form as

$$\phi_i = \exp(\Phi_i), \qquad \psi_j = \exp(\Psi_j), \tag{2.4}$$

where the phases Φ_i and Ψ_j are linear combinations of the independent variables z_k. By constructing a Gram-type matrix whose entries are formed from combinations of these eigenfunctions, one obtains a determinant tau function that satisfies the bilinear KP equations. Following this standard procedure, the tau function can be written in the Gram-determinant form given in Eq (2.1). For more details on this construction, we refer the reader to [35–37]. Next, by performing the variable transformation

$$z_1 = \frac{\mathrm{i}}{(-\beta)^{\frac{1}{4}}}x, \quad z_2 = 3\,\mathrm{i}\,t, \quad z_3 = 0, \tag{2.5}$$

the bilinear Eq (2.3) is converted into the bilinear form Eq (1.8), where the identification $\tau_0 = \mathfrak{g}$ is made. Consequently, the determinant expressions obtained above provide explicit solutions to the bilinear equation. In this framework, since u_0 is an arbitrary constant solution, we set $u_0 = -\frac{\sqrt{-\beta}}{2\alpha}$ without loss of generality for $\beta < 0$. Collecting these observations, we conclude that the determinant-type solutions of the bilinear form Eq (1.8) can be written as follows:

$$\mathfrak{g} = \left|\beta_{i,j} + \frac{p_i+q_i}{p_i+q_j}\exp\big(\Phi_i+\Psi_j\big)\right|_{1\le i,j\le N}, \tag{2.6}$$

where

$$\Phi_i = \frac{2\,\mathrm{i}p_i^3}{(-\beta)^{\frac{1}{4}}}x + \mathrm{i}p_i^2\sqrt{3}\,t + \frac{\mathrm{i}p_i}{2(-\beta)^{\frac{1}{4}}}x + \Phi_{i,0}, \quad \Psi_j = \frac{2\mathrm{i}q_j^3}{(-\beta)^{\frac{1}{4}}}x - \mathrm{i}q_j^2\sqrt{3}\,t + \frac{\mathrm{i}q_j}{2(-\beta)^{\frac{1}{4}}}x + \Psi_{j,0}, \tag{2.7}$$

under the condition

$$p_k^2 - p_k q_k + q_k^2 = \frac{1}{4}. \tag{2.8}$$

To satisfy the reduction from the KP hierarchy to the AB-BO equation, the parameters p_k and q_k cannot be arbitrary; they must satisfy the algebraic constraint Eq (2.8), which ensures that the soliton solutions obtained from the KP tau function satisfy the bilinear form of AB-BO Eq (1.8). This condition naturally arises from substituting the N-soliton determinant solution Eq (2.6) into the bilinear equation and requiring it to be valid.

2.1. *Breather waves*

We now turn to the derivation of breather wave solutions for Eq (1.8). To this end, we restrict attention to determinants of even dimension by choosing $N = 2M$ and imposing a specific set of parameter relations in Eq (2.6), given by

$$\begin{aligned} p_{2k-1} &= -\,\Omega_k + \frac{\omega_k}{2}, \quad p_{2k} = -\Omega_k^* - \frac{\omega_1}{2}, \quad \Phi_{2k-1,0} = \theta_{k_0}, \quad \Phi_{2k,0} = \theta_{k_0}^*, \\ q_{2k-1} &= \Omega_k + \frac{\omega_k}{2}, \quad q_{2k} = \Omega_k^* - \frac{\omega_1}{2}, \quad \Psi_{2k-1,0} = \eta_{k_0}, \quad \Psi_{2k,0} = \eta_{k_0}^*. \end{aligned} \tag{2.9}$$

Here, k and M are positive integers, ω_k are real-valued parameters, and Ω_k denote complex constants, with the superscript "(*)" indicating complex conjugation. With these constraints, one can show, following arguments similar to those presented in [38], that the tau function $\mathfrak{g}$ defined in Eq (2.6) remains a real-valued and non-vanishing function. As a result of these parameter selections, we obtain explicit breather wave solutions of order M for the AB-BO Eq (1.6), which can be expressed in the following form:

$$A = u_0 + \frac{6\beta}{\alpha}[\ln \mathfrak{g}]_{xx} + \zeta_1[\ln \mathfrak{g}]_{xxx} + \zeta_2[\ln \mathfrak{g}]_{xxt}, \tag{2.10}$$

$$B = u_0 + \frac{6\beta}{\alpha}[\ln \mathfrak{g}]_{xx} - \zeta_1[\ln \mathfrak{g}]_{xxx} - \zeta_2[\ln \mathfrak{g}]_{xxt}, \tag{2.11}$$

in which the function $\mathfrak{g}$ is represented explicitly by the determinant given as follows:

$$\mathfrak{g} = \Gamma \begin{bmatrix} \mathcal{G}_{1,1} & \mathcal{G}_{1,2} & \cdots & \mathcal{G}_{1,M} \\ \mathcal{G}_{2,1} & \mathcal{G}_{2,2} & \cdots & \mathcal{G}_{2,M} \\ \vdots & \vdots & \ddots & \vdots \\ \mathcal{G}_{M,1} & \mathcal{G}_{M,2} & \cdots & \mathcal{G}_{M,M} \end{bmatrix}, \tag{2.12}$$

with

$$\begin{aligned} &\mathcal{G}_{k,k} = \begin{bmatrix} \frac{1}{\omega_k e^{\phi_k}} + \frac{1}{\omega_k} & -\frac{1}{\Omega_k - \Omega_k^*} \\ -\frac{1}{\Omega_k - \Omega_k^*} & \frac{1}{\omega_k e^{\phi_k^*}} + \frac{1}{\omega_k} \end{bmatrix}, \quad \mathcal{G}_{k,j} = \begin{bmatrix} \frac{1}{\Omega_j - \Omega_k + \frac{\omega_k}{2} + \frac{\omega_j}{2}} & \frac{1}{\Omega_j^* - \Omega_k + \frac{\omega_k}{2} - \frac{\omega_j}{2}} \\ \frac{1}{\Omega_k^* - \Omega_j + \frac{\omega_k}{2} - \frac{\omega_j}{2}} & \frac{1}{\Omega_k^* - \Omega_j^* + \frac{\omega_k}{2} + \frac{\omega_j}{2}} \end{bmatrix}, \\ &\Gamma = \exp\left(\sum_{k=1}^{M} \phi_k + \phi_k^*\right) \prod_{k=1}^{M} \omega_k^2, \quad \phi_k = \mathrm{i}\,\omega_k \left(\frac{x}{(-\beta)^{\frac{1}{4}}} + 2\sqrt{3}\,\Omega_k\, t\right) + \kappa_k, \quad \kappa_k = \eta_{k_0} + \theta_{k_0}, \end{aligned} \tag{2.13}$$

where $\beta < 0$ and κ_k are arbitrary complex parameters, with the constraint $12\Omega_k^2 + \omega_k^2 = 1$. Let $\Omega_k = a_k + \mathrm{i}\, b_k$, then Ω_k is purely real with $a^2 \leq \frac{1}{12}$, or Ω_k is purely imaginary with no upper bound (since $1 + 12b^2 > 0$). It is worth mentioning that the breather waves are aligned parallel to the x-axis, that is,

$$t = \frac{\sqrt{3}\,\Re(\kappa_k)}{12\, b_k \sqrt{12 b_k^2 + 1}}, \tag{2.14}$$

where $\Re(\kappa_k)$ denotes the real part of κ_k. The period of the waves in the x-direction is given by

$$T_x = \frac{2\pi(-\beta)^{\frac{1}{4}}}{\sqrt{12 b_k^2 + 1}}. \tag{2.15}$$

If $\alpha > 0$, the solution corresponds to dark waves, whereas for $\alpha < 0$, it corresponds to bright waves. In addition, the parameters α and β directly affect the amplitude of the waves. By choosing $M = 1$ in the solution sets in Eqs (2.10) and (2.11), one obtains the fundamental (first-order) breather-type solution. In this case, the corresponding function $\mathfrak{g}$ takes the form

$$\mathfrak{g}_1 = 1 + \mathrm{e}^{\phi_1} + \mathrm{e}^{\phi_1^*} + \left(1 - \frac{\omega_1^2}{(\Omega_1^* - \Omega_1)^2}\right)\mathrm{e}^{\phi_1+\phi_1^*}, \tag{2.16}$$

where the phase variable ϕ_1 is defined as

$$\phi_1 = \mathrm{i}\,\omega_1\left(\frac{x}{(-\beta)^{\frac{1}{4}}} + 2\sqrt{3}\,\Omega_1\,t\right) + \kappa_1, \tag{2.17}$$

where $12\Omega_1^2 + \omega_1^2 = 1$ and $\beta < 0$. When the fields A and B are reconstructed through Eqs (2.10) and (2.11) and interpreted as a wave solution of breather type, the roles of the parameters ζ_1 and ζ_2 can be understood in terms of spatial and spatiotemporal modulation effects. The leading term $\frac{6\beta}{\alpha}(\ln f)_{xx}$ governs the fundamental balance between nonlinearity and dispersion and is responsible for the formation of localized structures such as solitons or breathers. The third-order spatial derivative term proportional to ζ_1 introduces a higher-order dispersion, which breaks the left-right spatial symmetry of the solution and induces a directional bias, leading to asymmetric profiles or a drift of the breather envelope; increasing $|\zeta_1|$ enhances this asymmetry and may cause gradual deformation or radiation from the breather. The mixed derivative term proportional to ζ_2 couples spatial location to temporal evolution and primarily affects the internal oscillatory dynamics of the breather, modifying its breathing frequency, group velocity, and amplitude modulation without strongly breaking spatial symmetry. For small values of ζ_2, the breather remains coherent with a shifted oscillation period, whereas larger values can intensify the breathing motion and eventually destabilize the localized structure. When both parameters are present, ζ_1 mainly controls spatial asymmetry and the propagation direction, while ζ_2 regulates temporal modulation. Their combined effect determines the qualitative features of the breather wave.

Figure 1 illustrates two different selections of ζ_1 and ζ_2. For $\zeta_1 = \zeta_2 = 0$, panel (a) shows a symmetric and stationary breather profile, which can be regarded as a solution of the classical BO equation. In contrast, for nonzero values of ζ_i, panels (b) and (c) display pronounced asymmetry and enhanced temporal modulation, highlighting the significant influence of higher-order dispersive effects on the breather dynamics. It is worth noting that the breather wave is obtained by choosing Ω_1 as a purely imaginary parameter together with $\beta < 0$. In contrast, when Ω_1 is taken as a purely real parameter, the solution in Eq (2.16) describes a mixed interaction of two soliton lines, as illustrated in Figure 2 for different values of ζ_1 and ζ_2.

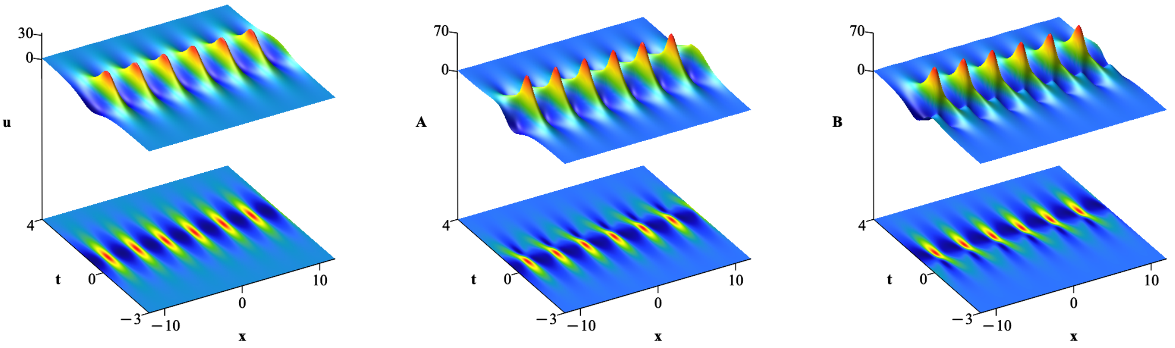

(a) (b) (c)

Figure 1. One-breather solution Eq (2.16) of the second-order AB–BO system with parameters $\alpha = -\frac{1}{4}$, $\beta = -\frac{2}{3}$, $\Omega_1 = \frac{\mathrm{i}}{3}$, and $\kappa_1 = \frac{1}{2} + \frac{\mathrm{i}\sqrt{3}}{2}$. In panel (a) $\zeta_1 = \zeta_2 = 0$: symmetric classical breather profile, and panels (b) and (c) $\zeta_1 = 5, \zeta_2 = 20$: asymmetric and temporally modulated breather structures induced by higher-order dispersive effects.

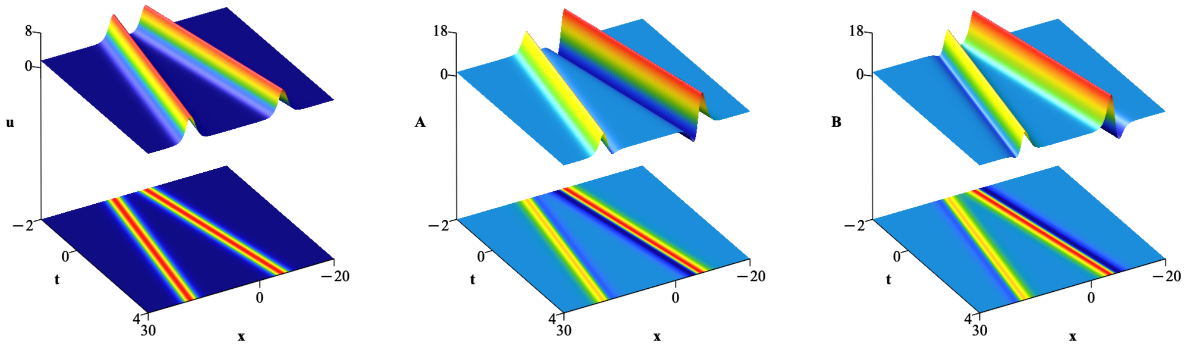

(a) (b) (c)

Figure 2. One-soliton solution Eq (2.16) obtained for real Ω_1 with parameters $\alpha = -\frac{1}{4}$, $\beta = -\frac{2}{3}$, $\Omega_1 = \frac{3}{7}$, and $\kappa_1 = 15$. In panel (a) $\zeta_1 = \zeta_2 = 0$: symmetric soliton, and panels (b) and (c) $\zeta_1 = 15, \zeta_2 = 30$: asymmetric deformation and spatiotemporal modulation due to higher-order terms.

Increasing the parameter M yields higher-order breather solutions for the AB-BO system (1.6). As a representative example, taking $M = 2$ leads to explicit two-breather configurations for the model, which can be written in the following form:

$$\begin{aligned}\mathfrak{g}_2 =& 1 + \mathrm{e}^{\phi_1} + \mathrm{e}^{\phi_2} + \mathrm{e}^{\phi_1^*} + \mathrm{e}^{\phi_2^*} + C_{1,1}\mathrm{e}^{\phi_1+\phi_1^*} + C_{2,2}\mathrm{e}^{\phi_2+\phi_2^*} + \hat{C}_{1,2}\mathrm{e}^{\phi_1+\phi_2} + \tilde{C}_{1,2}\mathrm{e}^{\phi_1+\phi_2^*} + \hat{C}_{1,2}^*\mathrm{e}^{\phi_1^*+\phi_2^*} \\ &+ \tilde{C}_{1,2}^*\mathrm{e}^{\phi_2+\phi_1^*} + C_{1,1}\hat{C}_{1,2}\tilde{C}_{1,2}^*\mathrm{e}^{\phi_1+\phi_2+\phi_1^*} + C_{2,2}\hat{C}_{1,2}\tilde{C}_{1,2}\mathrm{e}^{\phi_1+\phi_2+\phi_2^*} + C_{1,1}\hat{C}_{1,2}^*\tilde{C}_{1,2}\mathrm{e}^{\phi_1+\phi_1^*+\phi_2^*} \\ &+ C_{2,2}\hat{C}_{1,2}^*\tilde{C}_{1,2}^*\mathrm{e}^{\phi_2+\phi_1^*+\phi_2^*} + C_{1,1}C_{2,2}\hat{C}_{1,2}\tilde{C}_{1,2}\hat{C}_{1,2}^*\tilde{C}_{1,2}^*\mathrm{e}^{\phi_1+\phi_2+\phi_1^*+\phi_2^*},\end{aligned} \tag{2.18}$$

where

$$
\begin{aligned}
C_{1,1} =& 1-\frac{\omega_1^2}{(\Omega_1^*-\Omega_1)^2}, \quad C_{2,2} = 1-\frac{\omega_2^2}{(\Omega_2^*-\Omega_2)^2},\\
\hat{C}_{1,2} =& \frac{4(\Omega_1-\Omega_2)^2-(\omega_1-\omega_2)^2}{4(\Omega_1-\Omega_2)^2-(\omega_2+\omega_1)^2}, \quad \tilde{C}_{1,2} = \frac{4(\Omega_2^*-\Omega_1)^2-(\omega_2+\omega_1)^2}{4(\Omega_2^*-\Omega_1)^2-(\omega_1-\omega_2)^2}.
\end{aligned}
\tag{2.19}
$$

Similar to the case $M = 1$, different selections of the parameters Ω_i lead to different waveforms. When Ω_i are chosen as purely imaginary, the solution represents breather waves, whereas for purely real values of Ω_i the solution reduces to soliton waves. Figure 3 illustrates a double-breather wave structure, while Figure 4 depicts the interaction between breather and soliton lines.

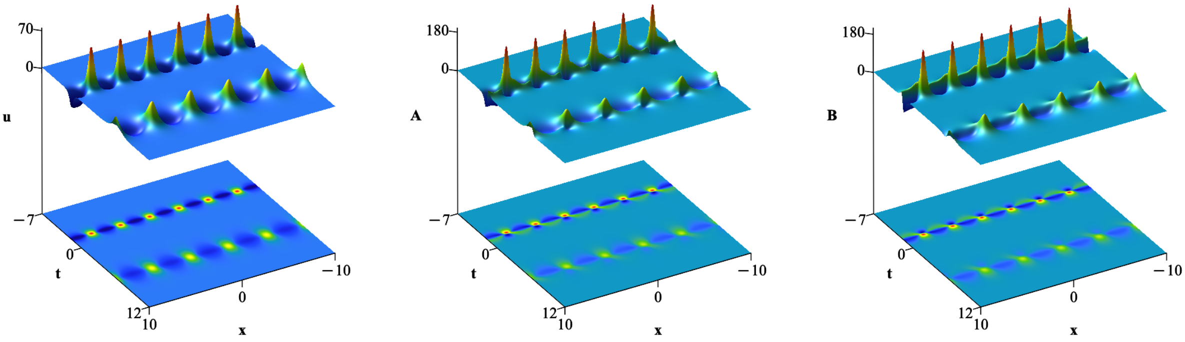

(a) (b) (c)

Figure 3. Two-breather solution Eq (2.18) with parameters $\alpha = -\frac{1}{4}$, $\beta = -1$, $\Omega_1 = \frac{i}{2}$, $\Omega_2 = \frac{i}{3}$, $\kappa_1 = -5$, and $\kappa_2 = 10$. In panel (a) $\zeta_1 = \zeta_2 = 0$: symmetric breather interaction, and panels (b) and (c) $\zeta_1 = 5$, $\zeta_2 = 20$: distorted and asymmetric breather interaction patterns.

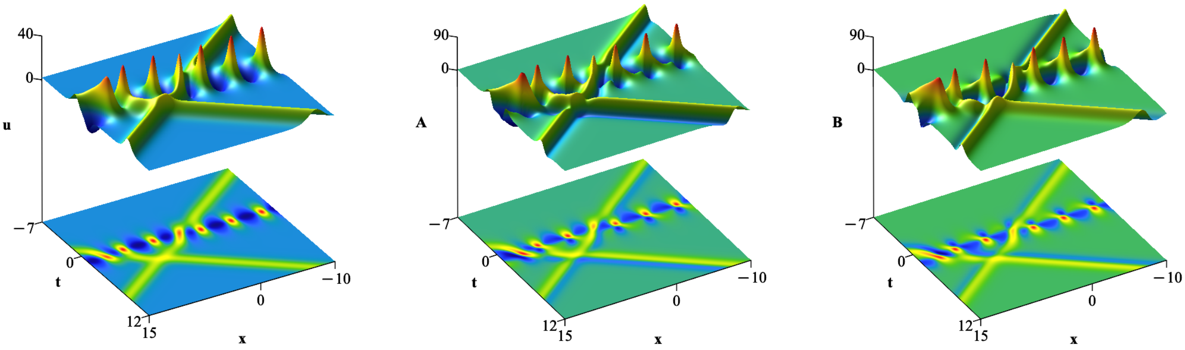

(a) (b) (c)

Figure 4. Breather-soliton interaction solution with parameters $\alpha = -\frac{1}{4}, \beta = -1$, $\Omega_1 = \frac{i}{2}$, $\Omega_2 = \frac{1}{3}$, $\kappa_1 = 0$, and $\kappa_2 = \frac{1}{2} + \frac{i}{3}$. In panel (a) $\zeta_1 = \zeta_2 = 0$: symmetric interaction, and panels (b) and (c) $\zeta_1 = 10, \zeta_2 = 35$: asymmetric and modulated breather-soliton dynamics.

Similarly, for $M = 3$, third-order breather solutions can be obtained, representing the combined dynamics of three interacting breathers. In this case, a variety of wave forms can also be generated by appropriate choices of the parameters Ω_k. Figure 5 illustrates the dynamics of these solutions for the field A, showing different configurations: a mixture of three breather waves, a combination of two solitons with two breathers, and one breather interacting with four solitons. These examples demonstrate the flexibility of the determinant approach in producing complex nonlinear wave patterns.

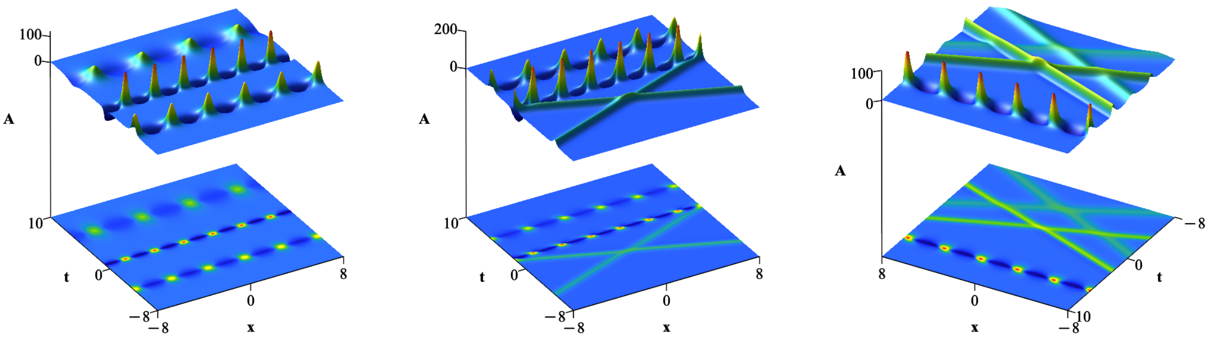

(a) **(b)** **(c)**

Figure 5. Third-order ($M = 3$) breather and breather-soliton configurations for different parameter choices: Panel (a) pure multi-breather interaction with $\alpha = -\frac{1}{4}, \beta = -1$, $\Omega_1 = \frac{i}{2}$, $\Omega_2 = \frac{i}{3}$, $\Omega_3 = \frac{2i}{3}$, $\Omega_4 = \frac{3i}{4}$, $\kappa_1 = -10$, $\kappa_2 = 10$, $\kappa_3 = 5$, $\kappa_4 = -15$, $\zeta_1 = 0$, $\zeta_2 = 0$; panel (b) mixed breather-soliton structure with $\alpha = -\frac{1}{4}$, $\beta = -1$, $\Omega_1 = -\frac{i}{2}$, $\Omega_2 = \frac{2i}{3}$, $\Omega_3 = \frac{2}{3}$, $\Omega_4 = \frac{3}{4}$, $\kappa_1 = -20$, $\kappa_2 = 10$, $\kappa_3 = 5$, $\kappa_4 = -15$; and panel (c) higher-order interaction pattern with $\alpha = -\frac{1}{4}, \beta = -1$, $\Omega_1 = -\frac{i}{2}$, $\Omega_2 = \frac{i}{2}$, $\Omega_3 = \frac{2}{3}$, $\Omega_4 = \frac{3}{4}$, $\kappa_1 = -20$, $\kappa_2 = 10, \kappa_3 = 5$, $\kappa_4 = -15$ when $\zeta_1 = \zeta_2 = 5$, demonstrating increased asymmetry and deformation.

2.2. *Semi-rational solutions (Interaction of breather and lump waves)*

By decomposing $M = \tilde{N} + \tilde{N}'$ and applying the long-wave limit [39] to the auxiliary function Eq (2.12), one can derive Mth-order semi-rational solutions consisting of a superposition of $\tilde{N}$th-order lumps (or rogue waves) and $\tilde{N}'$th-order breather (or soliton) structures. Specifically, when $\omega_k \to 0$, $(1 \le k \le \tilde{N})$, the exponential term degenerates into a polynomial form,

$$\lim_{\omega_k \to 0} \frac{1}{\omega_k}(1 + e^{-\phi_k}) = \frac{i}{(-\beta)^{\frac{1}{4}}} x + 2i\sqrt{3}\,\Omega_k t. \tag{2.20}$$

This limiting expression corresponds to the generation of $\tilde{N}$ lump waves. To ensure that the above limit exists, we set $\kappa_k = i\pi$. In summary, the function $\mathfrak{g}$ appearing in Eqs (2.10) and (2.11) can be expressed as a $2(\tilde{N}+\tilde{N}') \times 2(\tilde{N}+\tilde{N}')$ determinant, which provides a systematic way to construct a class of semi-rational solutions.

$$\mathfrak{g} = \begin{vmatrix} A & B \\ C & D \end{vmatrix}, \tag{2.21}$$

where A is the $2\tilde{N} \times 2\tilde{N}$ matrices given by

$$A_{k,k} = \begin{pmatrix} \theta_k & -\frac{1}{\Omega_k - \Omega_k^*} \\ -\frac{1}{\Omega_k - \Omega_k^*} & \theta_k^* \end{pmatrix}, \quad A_{k,l} = \begin{pmatrix} \frac{1}{-\Omega_k + \Omega_l} & \frac{1}{-\Omega_k + \Omega_l^*} \\ \frac{1}{\Omega_k^* - \Omega_l} & \frac{1}{\Omega_k^* - \Omega_l^*} \end{pmatrix}. \tag{2.22}$$

D is the $2\tilde{N}' \times 2\tilde{N}'$ matrices defined by

$$D_{k,k} = \begin{pmatrix} \frac{1}{\omega_k e^{\phi_k}} + \frac{1}{\omega_k} & -\frac{1}{\Omega_k - \Omega_k^*} \\ -\frac{1}{\Omega_k - \Omega_k^*} & \frac{1}{\omega_k e^{\phi_k^*}} + \frac{1}{\omega_k} \end{pmatrix}, \quad D_{k,l} = \begin{pmatrix} \frac{1}{(\Omega_k - \Omega_l) - \frac{\omega_k + \omega_l}{2}} & \frac{1}{-(\Omega_k - \Omega_l^*) + \frac{\omega_k - \omega_l}{2}} \\ \frac{1}{(\Omega_k^* - \Omega_l) + \frac{\omega_k - \omega_l}{2}} & \frac{1}{(\Omega_k^* - \Omega_l^*) + \frac{\omega_k + \omega_l}{2}} \end{pmatrix}. \tag{2.23}$$

B and C are $2\tilde{N} \times 2\tilde{N}'$ matrices and $2\tilde{N}' \times 2\tilde{N}$ matrices, respectively, defined by

$$B_{k,l} = \begin{pmatrix} \frac{1}{-(\Omega_k - \Omega_l) + \frac{\omega_l}{2}} & \frac{1}{-(\Omega_k - \Omega_l^*) + \frac{\omega_l}{2}} \\ \frac{1}{(\Omega_k^* - \Omega_l) + \frac{\omega_l}{2}} & \frac{1}{(\Omega_k^* - \Omega_l^*) + \frac{\omega_l}{2}} \end{pmatrix}, \quad C_{k,l} = \begin{pmatrix} \frac{1}{-(\Omega_k - \Omega_l) + \frac{\omega_k}{2}} & \frac{1}{-(\Omega_k + \Omega_l^*) + \frac{\omega_k}{2}} \\ \frac{1}{(\Omega_k^* - \Omega_l) + \frac{\omega_k}{2}} & \frac{1}{(\Omega_k^* - \Omega_l^*) + \frac{\omega_k}{2}} \end{pmatrix}, \tag{2.24}$$

with

$$\theta_k = \frac{\mathrm{i}}{(-\beta)^{\frac{1}{4}}} x + 2\mathrm{i}\sqrt{3}\,\Omega_k t, \tag{2.25}$$

$$\phi_k = \mathrm{i}\left(\frac{x}{(-\beta)^{\frac{1}{4}}} + 2\sqrt{3}\,\Omega_k\, t\right)\omega_k + \kappa_k. \tag{2.26}$$

By setting $\tilde{N} = \tilde{N}' = 1$ in solution Eq (2.21), the fundamental mixed solution can be obtained. Drawing on the previous analysis of periodic-wave and rational solutions, this mixed solution reveals the interaction between a lump (or rogue) and a breather (or soliton wave). In this context, the corresponding auxiliary function $\mathfrak{g}$ can be simplified and expressed in the following form:

$$\mathfrak{g} = \begin{vmatrix} \theta_1 & \frac{1}{\Omega_1^* - \Omega_1} & \frac{1}{\Omega_2 - \Omega_1 + \frac{\omega_2}{2}} & \frac{1}{\Omega_2^* - \Omega_1 + \frac{\omega_2}{2}} \\ \frac{1}{\Omega_1^* - \Omega_1} & \theta_1^* & \frac{1}{\Omega_1^* - \Omega_2 + \frac{\omega_2}{2}} & \frac{1}{\Omega_2^* + \Omega_1^* + \frac{\omega_2}{2}} \\ \frac{1}{\Omega_2 - \Omega_1 + \frac{\omega_2}{2}} & \frac{1}{\Omega_2^* - \Omega_1 + \frac{\omega_2}{2}} & \frac{1}{\omega_2 e^{\phi_2}} + \frac{1}{\omega_2} & \frac{1}{\Omega_2^* - \Omega_2} \\ \frac{1}{\Omega_1^* - \Omega_2 + \frac{\omega_2}{2}} & \frac{1}{\Omega_1^* - \Omega_2^* + \frac{\omega_2}{2}} & \frac{1}{\Omega_2^* - \Omega_2} & \frac{1}{\omega_2 e^{\phi_2^*}} + \frac{1}{\omega_2} \end{vmatrix}. \tag{2.27}$$

Here, ϕ_2 is defined by Eq (2.26), and the parameters Ω_2 and ω_2 are constrained by the relation $12\Omega_2^2 + \omega_2 = 1$. Depending on the choice of Ω_2, the semi-rational solution exhibits different behaviors: When the real part of Ω_2 vanishes, a single rogue wave coexists with a breather; whereas for $\Omega_{2R} \neq 0$, the rogue wave interacts with a soliton wave. Figures 6 and 7 illustrate these two distinct types of mixed solutions for the AB-BO system.

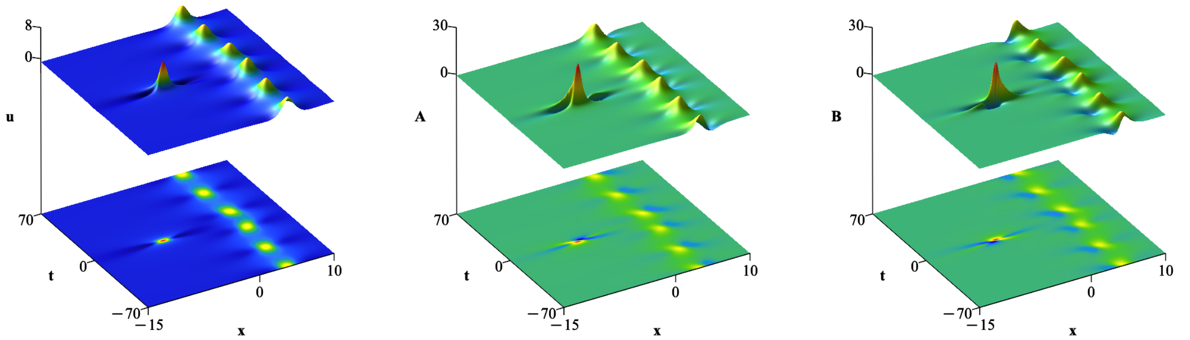

(a) (b) (c)

Figure 6. Semi-rational one-breather-one-lump solution with parameters $\alpha = -\frac{1}{3}, \beta = -\frac{1}{3}$, $\Omega_2 = \frac{3i\sqrt{3}}{20}$, and $\kappa_2 = \frac{\pi}{2}$. In panel (a) $\zeta_1 = \zeta_2 = 0$: symmetric interaction, and panels (b) and (c) $\zeta_1 = 2$, $\zeta_2 = 5$: asymmetric breather-lump interaction.

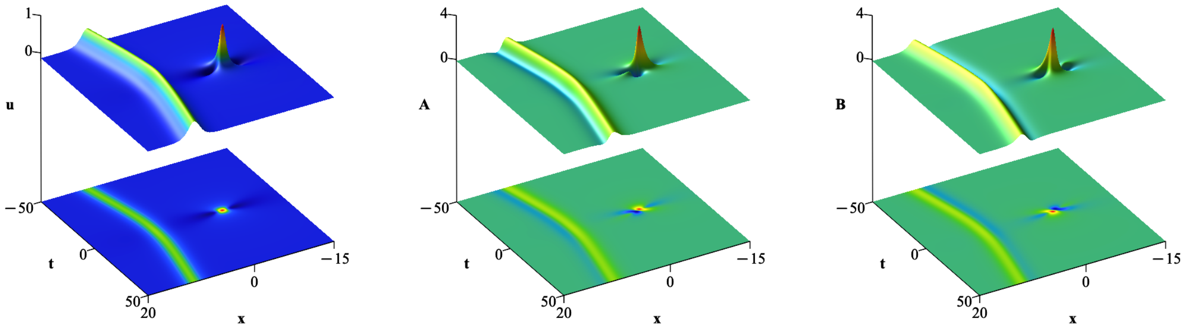

(a) (b) (c)

Figure 7. Semi-rational one-soliton-one-lump solution with parameters $\alpha = -2, \beta = -\frac{1}{3}$, $\Omega_2 = \frac{1}{20}$, and $\kappa_2 = 10$. In panel (a) $\zeta_1 = \zeta_2 = 0$: symmetric interaction and panels (b) and (c) $\zeta_1 = 2$, $\zeta_2 = 5$: asymmetric soliton-lump interaction.

The results presented in this section demonstrate the effectiveness of the determinant framework in generating a broad class of exact solutions for the second-order AB-BO system. Through appropriate parameter selections and long-wave limits, we have shown that the model admits pure breather solutions, multi-breather interactions, and semi-rational structures that describe the coexistence and interactions of breathers, solitons, and lump waves. The flexibility of the block-determinant formulation allows for the systematic construction of increasingly complex wave patterns while preserving integrability. These findings not only reveal rich interaction dynamics inherent in the nonlocal AB structure but also lay the foundation for the construction of fully rational rogue wave solutions, which will be developed in the next section.

3. Higher-order rogue waves

Rogue waves represent one of the most striking manifestations of nonlinear wave dynamics, characterized by their extreme amplitude, strong localization in space and time, and sudden appearance from a continuous background. In the context of nonlocal integrable systems, such as the second-order AB-BO equation, rogue waves exhibit additional structural complexity due to the intrinsic two-place correlations between the fields. Motivated by the rich breather and semi-rational structures obtained in the previous section, we now turn to the systematic construction of higher-order rogue wave solutions. By combining bilinear theory with Schur polynomial techniques, we derive compact determinant representations that allow us to analyze their detailed spatiotemporal patterns and geometric configurations.

One of the requirements for constructing algebraic rogue wave solutions is the use of Schur polynomials. These are defined through the generating function

$$\sum_{n=0}^{\infty} \mathcal{S}_n(y)\lambda^n = \exp\left(\sum_{k=1}^{\infty} y_k \lambda^k\right), \tag{3.1}$$

which generates a sequence of symmetric polynomials $\mathcal{S}_n(y)$ in the infinite variable set $y = (y_1, y_2, y_3, \cdots)$. These functions arise naturally in the study of integrable systems and symmetric functions. Expanding the exponential leads to an explicit formula

$$\mathcal{S}_n(y) = \sum_{\substack{l_1, l_2, \cdots \geq 0 \\ l_1 + 2l_2 + \cdots = n}} \prod_{j=1}^{n} \frac{y_j^{l_j}}{l_j!}, \tag{3.2}$$

where the sum runs over all nonnegative integer sequences $(l_1, l_2, \dots)$ such that the weighted sum equals n. This formula resembles the exponential generating function for complete symmetric functions. For example,

$$\mathcal{S}_0(y) = 1, \ \ \mathcal{S}_1(y) = y_1, \ \ \mathcal{S}_2(y) = \frac{1}{2}y_1^2 + y_2, \ \ \mathcal{S}_3(y) = \frac{1}{6}y_1^3 + y_1 y_2 + y_3, \cdots. \tag{3.3}$$

In particular, the given exponential generating function corresponds to the vacuum tau-function of the KP hierarchy. Through the KP reduction method, more general exact solutions can be obtained by modifying or composing such generating functions, making $\mathcal{S}_n(y)$ a fundamental tool in constructing solutions to the KP equations. With the Schur polynomials and the bilinear form of the AB-BO system established, we are now equipped to construct explicit rogue wave solutions. The following theorem summarizes this construction and provides a general formula for the rogue wave solutions.

Theorem 1. *Upon choosing the arbitrary seed solution* $u_0 = \frac{6\sqrt{-\beta}}{\alpha}$ *for* $\beta < 0$*, the general higher-order rogue wave solutions in the second-order AB-BO system* (1.6) *are*

$$\begin{aligned} A_n &= \frac{6\sqrt{-\beta}}{\alpha} - \frac{6\beta}{\alpha}[\ln\tau]_{xx} + \zeta_1[\ln\tau]_{xxx} + \zeta_2[\ln\tau]_{xxt}, \\ B_n &= \frac{6\sqrt{-\beta}}{\alpha} - \frac{6\beta}{\alpha}[\ln\tau]_{xx} - \zeta_1[\ln\tau]_{xxx} - \zeta_2[\ln\tau]_{xxt}, \end{aligned} \tag{3.4}$$

where

$$\tau(x,t) = \det_{1\le i,j\le n}\left(\phi_{2i-1,\,2j-1}\right), \tag{3.5}$$

and

$$\phi_{i,j} = \sum_{\nu=0}^{\min(i,j)} \left(-\frac{1}{12}\right)^{\nu} \mathcal{S}_{i-\nu}(\mathbf{X}^{+} + \nu\mathbf{h})\,\mathcal{S}_{j-\nu}(\mathbf{X}^{-} + \nu\mathbf{h}). \tag{3.6}$$

Vectors $\mathbf{X}^{\pm} = (\mathcal{X}_1^{\pm}, \mathcal{X}_2^{\pm}, \ldots)$ and $\mathbf{h} = (h_1,\, h_2,\, \ldots)$ are defined as

$$\mathcal{X}_{2r+1}^{+} = \frac{\mathrm{i}}{3^{2r+\frac{1}{2}}(2r+1)!}\left(\beta^{-\frac{1}{4}}x + \sqrt{3}\,2^{2r+1}\mathrm{i}\,t\right) + a_{2r+1}, \quad r = 0,1,2,\ldots \tag{3.7a}$$

$$\mathcal{X}_{2r+1}^{-} = \frac{\mathrm{i}}{3^{2r+\frac{1}{2}}(2r+1)!}\left(\beta^{-\frac{1}{4}}x - \sqrt{3}\,2^{2r+1}\mathrm{i}\,t\right) - a_{2r+1}^{*}, \quad r = 0,1,2,\ldots \tag{3.7b}$$

$$\mathcal{X}_{2r}^{\pm} = 0, \quad r = 1,2,3,\ldots \tag{3.7c}$$

The first few h_k values are:

$$\left[\; h_1 = \tfrac{2\mathrm{i}}{9}\sqrt{3} \quad h_2 = -\tfrac{5}{108} \quad h_3 = -\tfrac{5\mathrm{i}}{729}\sqrt{3} \quad h_4 = \tfrac{287}{116640} \quad h_5 = \tfrac{17\mathrm{i}}{43740}\sqrt{3} \;\right]. \tag{3.8}$$

These coefficients are obtained from the generating function:

$$\sum_{r=1}^{\infty} h_r \lambda^r = \ln\left[\frac{2\mathrm{i}\sqrt{3}}{\lambda}\tanh\left(\frac{\lambda}{6}\right)\tanh\left(\frac{\lambda}{6} + \frac{2\pi\mathrm{i}}{3}\right)\right]. \tag{3.9}$$

Here, a_i are arbitrary complex parameters, a_i^* denotes the complex conjugate of a_i, and $\mathrm{i} = \sqrt{-1}$. The parameter $\beta < 0$, while α is an arbitrary nonzero real constant, which guarantees that the rogue wave solutions remain non-singular. When $\alpha < 0$, the solution corresponds to a bright rogue wave, whereas for $\alpha > 0$, it corresponds to a dark rogue wave. Moreover, the parameters α and β determine the wave background and directly influence the wave amplitude.

Proof. The proof of this theorem follows a similar approach to that outlined in [40–42], and is therefore omitted here. □

We emphasize that the condition $\beta < 0$ in the general solutions Eq (3.4) is consistent with the requirement for the existence of rogue waves for the second-order BO equation as reported in [25, 43, 44].

Proposition 1. *The parameters a_i do not influence the amplitudes of the rogue wave peaks for any choice of ζ_1 and ζ_2. Instead, a_i only controls the spatiotemporal locations of the rogue wave peaks.*

Dynamics of higher-order rogue waves

We analyze the dynamical behavior of the higher-order rational solution τ_n by utilizing the matrix entries given in Eq (3.6). The simplest rogue wave, known as the Peregrine-type rogue wave, can be obtained by setting $n = 1$ in Theorem 1. By doing so, we can derive

$$A_1 = \frac{6\sqrt{-\beta}}{\alpha} + \frac{6\beta}{\alpha}[\ln\tau_1]_{xx} + \zeta_1[\ln\tau_1]_{xxx} + \zeta_2[\ln\tau_1]_{xxt}, \tag{3.10}$$

$$B_1 = \frac{6\sqrt{-\beta}}{\alpha} + \frac{6\beta}{\alpha}[\,\ln\tau_1]_{xx} - \zeta_1[\,\ln\tau_1]_{xxx} - \zeta_2[\,\ln\tau_1]_{xxt}, \tag{3.11}$$

in which

$$\tau_1 = -\frac{1}{3\sqrt{-\beta}}x^2 - \frac{2\sqrt{3}\,\Im(a_1)}{3(-\beta)^{\frac{1}{4}}}x - 4t^2 + 2\Re(a_1)t - |a_1|^2 - \frac{1}{12}, \tag{3.12}$$

where a_1 is an arbitrary complex parameter and $\Re(z)$ and $\Im(z)$ denote the real and imaginary parts of a complex number z, respectively.

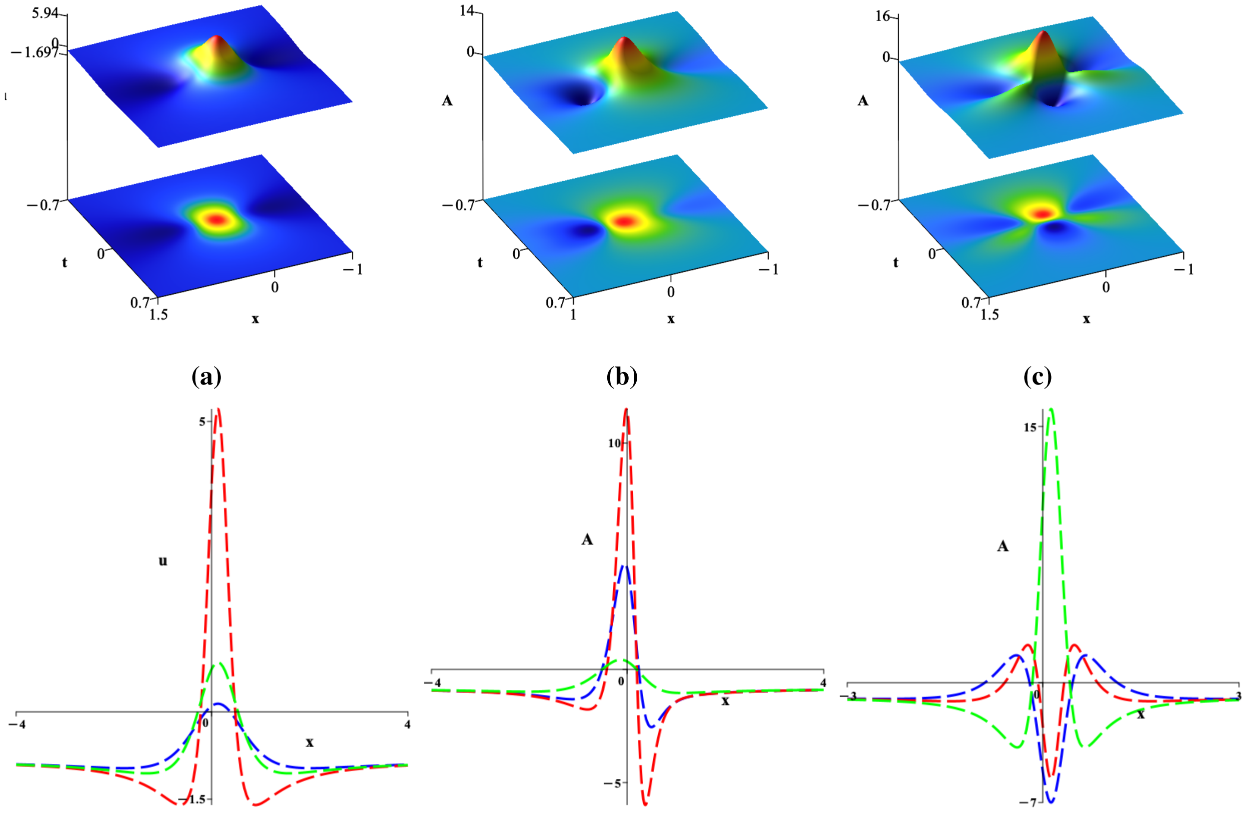

(a) (b) (c)

(d) (e) (f)

Figure 8. First-order (Peregrine-type) rogue wave solution with parameters $\alpha = -5$, $\beta = -\frac{1}{2}$, and $a_1 = -\frac{1}{10} - \frac{i}{12}$. In panel (a) $\zeta_1 = \zeta_2 = 0$: symmetric rogue wave profile and time evolution; panel (b) $\zeta_1 = \frac{1}{4}, \zeta_2 = 0$: spatial asymmetry induced by third-order dispersion; and panel (c) $\zeta_1 = 0, \zeta_2 = \frac{1}{4}$: spatiotemporal tilting due to mixed derivative effects. Second row: corresponding spatial cross-sections at fixed times illustrating temporal evolution, where panel (d) $\zeta_1 = \zeta_2 = 0$ with $t = 0.3$ (blue), $t = 0$ (red), $t = -0.3$ (green); panel (e) $\zeta_1 = \frac{1}{4}$, $\zeta_2 = 0$ with $t = 0.1$ (blue), $t = 0$ (red), $t = -0.1$ (green); and panel (f) $\zeta_1 = 0$, $\zeta_2 = \frac{1}{4}$ with the same time slices, showing asymmetric growth and decay of the rogue event.

Figure 8 presents the spatiotemporal evolution of the first-order rogue wave solutions A_1 and B_1 for different values of the higher-order parameters ζ_1 and ζ_2. These parameters quantify deviations from the standard rogue-wave structure via higher-order spatial and spatiotemporal corrections. When $\zeta_1 = \zeta_2 = 0$, both components reduce to a symmetric rogue wave with identical profiles. In this case, the solution exhibits a single localized peak, accompanied by two symmetric depressions (holes) on either side. The maximum amplitude of the rogue wave attains the value

$$u_{\max} = -\frac{42\sqrt{-\beta}}{\alpha}, \tag{3.13}$$

which occurs at the spatiotemporal location

$$(x,t)_{\max} = \left(\sqrt{3}\,\Im(a_1)\,(-\beta)^{\frac{1}{4}},\ \frac{\Re(a_1)}{2}\right). \tag{3.14}$$

Meanwhile, the two adjacent holes reach their minimum amplitudes

$$u_{\min} = \frac{12\sqrt{-\beta}}{\alpha} \tag{3.15}$$

at symmetric spatial positions relative to the peak location, given as follows:

$$(x,t)_{\min} = \left(\sqrt{3}\,\Im(a_1)\,(-\beta)^{\frac{1}{4}} \pm \frac{\sqrt{3}\,(-\beta)^{\frac{1}{4}}}{2},\ \frac{\Re(a_1)}{2}\right). \tag{3.16}$$

These critical points confirm that the solution corresponds to a standard Peregrine-type rogue wave, characterized by maximal amplification over the continuous-wave background, algebraic localization in both space and time, and complete spatial and temporal symmetry. The wave emerges from the background, reaches its maximum amplitude at $(x,t)_{\max}$, and subsequently decays back to the background state.

When $\zeta_1 \neq 0$ and $\zeta_2 = 0$, the rogue wave structure becomes spatially asymmetric, as illustrated in panels (b) and (e) of Figure 8. The inclusion of the third-order spatial derivative term $(\ln\tau)_{xxx}$ breaks the left–right symmetry of the wave profile, leading to unequal side lobes and a skewed peak structure. This term plays a role analogous to higher-order dispersion or self-steepening effects in nonlinear dispersive media. Due to the opposite signs of the ζ_1 contributions in A_1 and B_1, the spatial skewness manifests in opposite directions for the two components, indicating a redistribution of energy between them. Despite this deformation, the rogue wave remains strongly localized and retains its extreme-amplitude character.

In contrast, when $\zeta_2 \neq 0$ and $\zeta_1 = 0$, the rogue wave exhibits pronounced spatiotemporal asymmetry, as shown in panels (c) and (f) of Figure 8. The peak becomes tilted in the x–t plane, and the growth and decay of the wave occur at different rates on either side of the localization center. The mixed derivative term $(\ln\tau)_{xxt}$ introduces a coupling between spatial curvature and temporal evolution, which may be interpreted as a higher-order dispersive correction inducing temporal acceleration or delay of the rogue event. As in the previous case, the opposite signs of the ζ_2 terms in A_n and B_n lead to complementary temporal behaviors in the two components. In general, the parameters ζ_1 and ζ_2 do not suppress the formation of rogue waves, but instead modulate their geometric structure and internal energy exchange. Specifically, ζ_1 controls spatial asymmetry associated with higher-order dispersion or self-steepening effects, whereas ζ_2 governs spatiotemporal tilting through space–time coupling. Their combined influence leads to drifting and distorted vector rogue waves, highlighting the rich dynamics induced by higher-order effects in multicomponent nonlinear systems.

In addition to the higher-order parameters ζ_1 and ζ_2, the rogue wave solution contains a free complex parameter a_1, which plays a purely geometrical role in the wave dynamics. Numerical inspection and analytical evaluation show that variations of a_1 do not affect the peak amplitude or the depth of the adjacent holes of the rogue wave. Instead, the parameter a_1 governs the spatial and temporal localization of the extreme event. Specifically, varying the real and imaginary parts of a_1 leads to a translation of the rogue wave peak in the x–t plane without changing its intrinsic profile, even when the parameters ζ_1 and ζ_2 are nonzero. This effect is illustrated in Figure 9, where different choices of a_1 generate rogue waves with identical maximum and minimum amplitudes but with peaks located at different spatiotemporal positions. This observation also confirms the validity of Proposition 1.

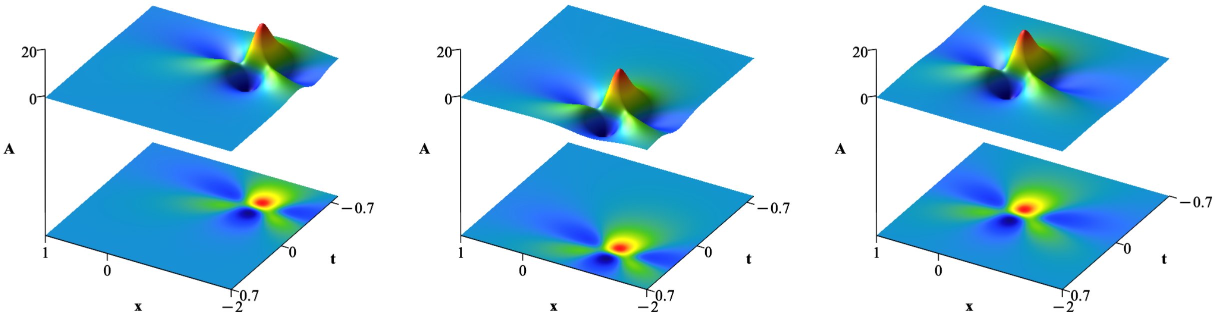

(a) $a_1 = -\frac{3}{4} + \frac{4\mathrm{i}}{5}$ **(b)** $a_1 = \frac{3}{4} + \frac{3\mathrm{i}}{4}$ **(c)** $a_1 = \frac{\mathrm{i}}{6}\sqrt{3}$

Figure 9. Influence of parameter a_1 on the localization of the first-order rogue wave with $\alpha = -5, \beta = -\frac{1}{2}, \zeta_1 = \frac{1}{30}$, and $\zeta_2 = \frac{1}{4}$. Different choices of a_1 shift the rogue wave peak position in the (x, t) plane without changing its amplitude.

To construct the second-order rogue wave solution, we set $n = 2$ in the general solutions Eq (3.4). In this case, the solution involves two free complex parameters, a_1 and a_3. When $a_1 = a_3 = 0$, the corresponding tau-function reduces to the following form:

$$\begin{aligned}\tau_2 =& \frac{16t^6}{27} + \left(\frac{11}{81} + \frac{4x^2}{27\sqrt{-\beta}} + \frac{16x}{81(-\beta)^{\frac{1}{4}}}\right)t^4 + \left(\frac{131}{3888} + \frac{x^4}{81\beta}\right.\\ &\left. + \frac{8x^3}{243(-\beta)^{\frac{3}{4}}} + \frac{31x^2}{486\sqrt{-\beta}} + \frac{5x}{81(-\beta)^{\frac{1}{4}}}\right)t^2 + \frac{73}{186624} + \frac{x^6}{2916\beta^{\frac{3}{2}}}\\ &+ \frac{x^5}{729\beta^{\frac{5}{4}}} + \frac{35x^4}{11664\beta} + \frac{11x^3}{2916(-\beta)^{\frac{3}{4}}} + \frac{107x^2}{46656\sqrt{-\beta}} + \frac{x}{1944(-\beta)^{\frac{1}{4}}}.\end{aligned} \tag{3.17}$$

The resulting second-order rogue wave profile is displayed in the first row of Figure 10. For other choices of the free parameters, the structure of the rogue wave undergoes significant changes. As an illustrative example, by selecting $a_1 = 1$ and $a_3 = 3$, the tau-function takes the form

$$\begin{aligned}\tau_2 =& \frac{16t^6}{27} - \frac{16t^5}{9} + \left(\frac{191}{81} + \frac{4x^2}{27\sqrt{-\beta}} + \frac{16x}{81(-\beta)^{\frac{1}{4}}}\right)t^4 - \left(\frac{110}{243} + \frac{8x^2}{27\sqrt{-\beta}} + \frac{32x}{81(-\beta)^{\frac{1}{4}}}\right)t^3 \\ &+ \left(-\frac{4501}{3888} + \frac{x^4}{81\beta} + \frac{8x^3}{243(-\beta)^{\frac{3}{4}}} + \frac{139x^2}{486\sqrt{-\beta}} + \frac{29x}{81(-\beta)^{\frac{1}{4}}}\right)t^2 + \left(\frac{6683}{11664} - \frac{x^4}{81\beta}\right. \\ &\left. - \frac{8x^3}{243(-\beta)^{\frac{3}{4}}} - \frac{25x^2}{54\sqrt{-\beta}} - \frac{433x}{729(-\beta)^{\frac{1}{4}}}\right)t + \frac{376375}{559872} + \frac{x^6}{2916\beta^{\frac{3}{2}}} + \frac{x^5}{729\beta^{\frac{5}{4}}} \\ &+ \frac{71x^4}{11664\beta} + \frac{35x^3}{2916(-\beta)^{\frac{3}{4}}} + \frac{8867x^2}{46656\sqrt{-\beta}} + \frac{1429x}{5832(-\beta)^{\frac{1}{4}}},\end{aligned} \tag{3.18}$$

and the corresponding solution is depicted in the second row of Figure 10.

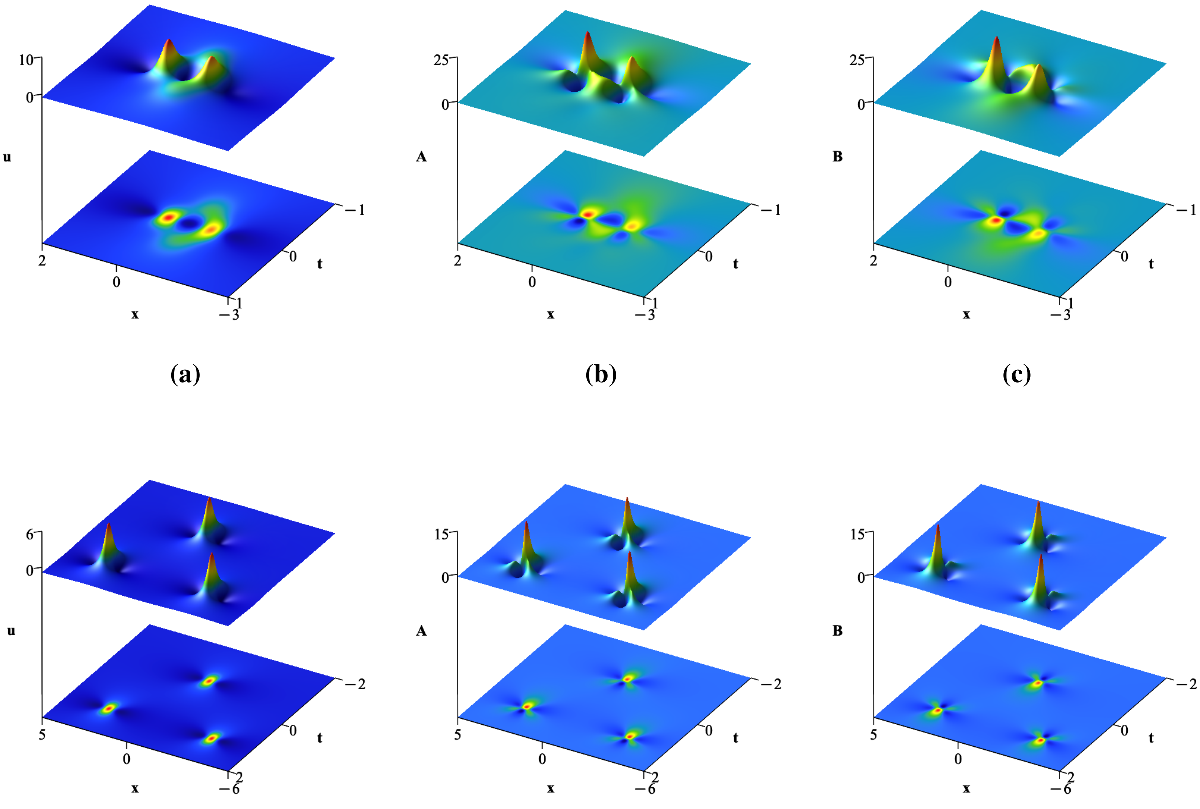

(a) (b) (c)

(d) (e) (f)

Figure 10. Second-order rogue wave solutions Eqs (3.17) and (3.18) with $\alpha = -5$ and $\beta = -\frac{1}{2}$, where panels (a)–(c) $a_1 = a_3 = 0$: symmetric two-peak configuration; panels (d)–(f) $a_1 = 1$, $a_3 = 5$: triangular three-peak rogue wave pattern. Panels compare symmetric ($\zeta_1 = \zeta_2 = 0$) and asymmetric $\left(\zeta_1 = \frac{1}{30}, \zeta_2 = \frac{1}{5}\right)$ cases.

The second-order rogue wave solutions A_2 and B_2, defined by Eqs (3.10)–(3.11), exhibit a wide range of spatiotemporal patterns that strongly depend on the free parameters a_i and the higher-order coefficients ζ_1 and ζ_2. Figure 10 compares the wave fields u, A, and B and clearly demonstrates how variations in these parameters affect the overall shape and structure of the rogue waves. For the parameter choice $a_1 = a_3 = 0$, shown in the first row of Figure 10, the second-order rogue wave is characterized by two dominant peaks that are symmetrically located in the (x, t) plane. This configuration can be regarded as the basic form of the second-order rogue wave, where the wave energy remains strongly localized and the interaction between the peaks is relatively compact. In this case, the logarithmic derivative terms in Eqs (3.10)–(3.11) generate a highly concentrated wave profile, while the absence of additional phase parameters prevents the peaks from separating further.

When the parameters are changed to $a_1 = 1$ and $a_3 = 3$, as illustrated in the second row of Figure 10, the rogue wave structure undergoes a noticeable transformation. The two-peak pattern evolves into a three-peak configuration, forming a triangular arrangement. This transition indicates that increasing the parameters a_i promotes the separation of the wave components. From a physical perspective, these parameters control the higher-order solution's internal degrees of freedom, redistributing energy in both space and time. As a result, the initially concentrated peaks split and reorganize into a triangular pattern, which is a well-known signature of higher-order rogue waves. This observation highlights the role of the parameters a_i in determining not only the number of peaks but also their spatial geometry. Figure 10 also reveals the influence of the higher-order coefficients ζ_1 and ζ_2. The field u, corresponding to $\zeta_1 = \zeta_2 = 0$, serves as a reference case in which the rogue wave remains symmetric and is mainly governed by second-order effects. In contrast, when $\zeta_i \neq 0$, as in the components A and B, the higher-order derivative terms $[\ln \tau_2]_{xxx}$ and $[\ln \tau_2]_{xxt}$ introduce asymmetry and directional deformation into the wave profiles. Due to the opposite signs of these terms in Eqs (3.10) and (3.11), the resulting structures of A and B display complementary behaviors, which is clearly reflected in their mirrored peak orientations. Setting $n = 3$ in Theorem 1, one obtains the third-order rogue wave solution. This solution contains three free complex parameters, denoted by a_j with $j = 1, 3, 5$. For the particular choice $a_1 = a_3 = a_5 = 0$ the associated tau-function takes the form

$$
\begin{aligned}
\tau_3 = & -\frac{64t^{12}}{54675} - \bigg(\frac{248}{164025} + \frac{32x^2}{54675\sqrt{-\beta}} + \frac{256x}{164025(-\beta)^{\frac{1}{4}}}\bigg)t^{10} - \bigg(\frac{587}{393660} + \frac{4x^4}{32805\beta} + \frac{64x^3}{98415(-\beta)^{\frac{3}{4}}} \\
& + \frac{166x^2}{98415\sqrt{-\beta}} + \frac{76x}{32805(-\beta)^{\frac{1}{4}}}\bigg)t^8 - \bigg(\frac{4393}{4723920} + \frac{4x^6}{295245\beta^{\frac{3}{2}}} + \frac{32x^5}{295245\beta^{5/4}} + \frac{131x^4}{295245\beta} + \frac{328x^3}{295245(-\beta)^{\frac{3}{4}}} \\
& + \frac{2131x^2}{1180980\sqrt{-\beta}} + \frac{713x}{393660(-\beta)^{\frac{1}{4}}}\bigg)t^6 - \bigg(\frac{21671}{1813988} + \frac{x^8}{118080\beta^2} + \frac{8x^7}{88535\beta^{\frac{7}{4}}} + \frac{35x^6}{708588\beta^{\frac{3}{2}}} + \frac{61x^5}{354294\beta^{\frac{5}{4}}} \\
& + \frac{2309x^4}{566704\beta} + \frac{1853x^3}{28352(-\beta)^{\frac{3}{4}}} + \frac{7643x^2}{113378\sqrt{-\beta}} + \frac{4519x}{113708(-\beta)^{\frac{1}{4}}}\bigg)t^4 + \bigg(-\frac{60983}{4353564672} - \frac{x^{10}}{35429400\beta^{5/2}} \\
& - \frac{x^9}{2657205\beta^{\frac{9}{4}}} - \frac{43x^8}{17006112\beta^2} - \frac{29x^7}{2657205\beta^{\frac{7}{4}}} - \frac{5579x^6}{170061120\beta^{\frac{3}{2}}} - \frac{12049x^5}{170061120\beta^{\frac{5}{4}}} - \frac{5033x^4}{453349632\beta} \\
& - \frac{2855x^3}{22674816(-\beta)^{\frac{3}{4}}} - \frac{36637x^2}{362797056\sqrt{-\beta}} - \frac{3113x}{60466176(-\beta)^{\frac{1}{4}}}\bigg)t^2 - \frac{47569}{417942208512} - \frac{x^{12}}{2550916800\beta^3} \\
& - \frac{x^{11}}{159432300\beta^{\frac{11}{4}}} - \frac{251x^{10}}{5101833600\beta^{\frac{5}{2}}} - \frac{25x^9}{102036672\beta^{\frac{9}{4}}} - \frac{6907x^8}{8162933760\beta^2} - \frac{4283x^7}{2040733440\beta^{\frac{7}{4}}} - \frac{30889x^6}{8162933760\beta^{\frac{3}{2}}} \\
& - \frac{8083x^5}{1632586752\beta^{\frac{5}{4}}} - \frac{40061x^4}{8707129344\beta} - \frac{18625x^3}{6530347008(-\beta)^{\frac{3}{4}}} - \frac{57563x^2}{52242776064\sqrt{\beta}} - \frac{353x}{1088391168(-\beta)^{\frac{1}{4}}}.
\end{aligned}
\tag{3.19}
$$

Similar to the second-order case, this parameter choice produces three interacting rogue wave peaks aligned along the t-axis, as shown in Figure 11. As the magnitudes of the free parameters a_j increase, these interacting waves gradually separate, eventually forming six distinct peaks. Figures 12 and 13 present different rogue wave configurations obtained for various parameter settings. In particular, when a_3 is taken to be relatively large while the remaining parameters remain small, the rogue waves arrange themselves into a triangular pattern (Figure 12). On the other hand, a dominant value of a_5 leads to the formation of a pentagonal rogue wave structure (Figure 13). In both scenarios, the peak amplitudes remain identical and coincide with that of the fundamental Peregrine-type rogue wave.

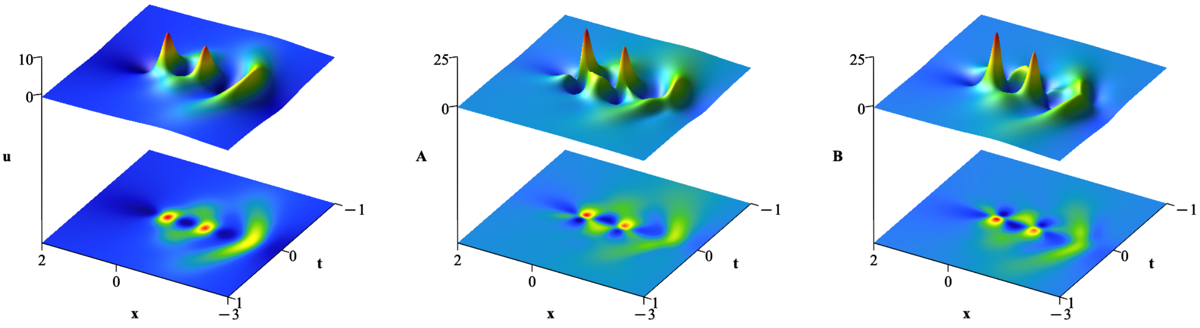

(a) **(b)** **(c)**

Figure 11. Third-order rogue wave solution Eq (3.19) with parameters $\alpha = -5$, $\beta = -\frac{1}{2}$, and $a_1 = a_3 = a_5 = 0$. In panel (a) $\zeta_1 = \zeta_2 = 0$: symmetric multi-peak structure, and panels (b) and (c) $\zeta_1 = \frac{1}{30}$, $\zeta_2 = \frac{1}{7}$: asymmetric deformation of interacting rogue peaks.

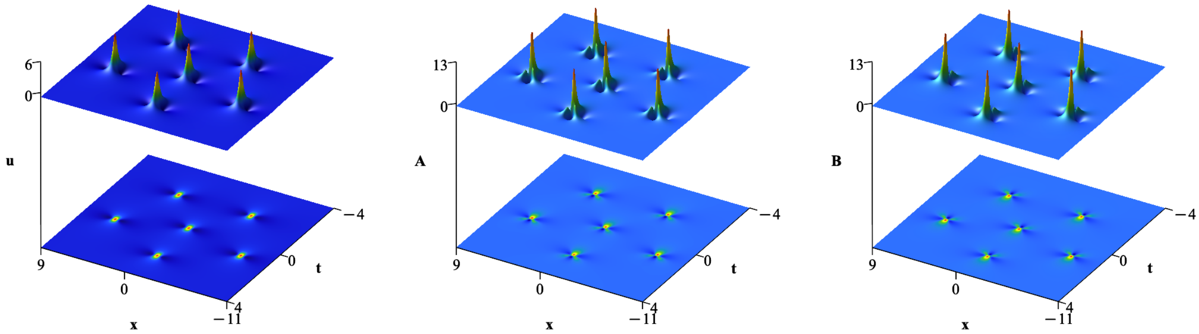

(a) **(b)** **(c)**

Figure 12. Third-order rogue wave exhibiting triangular configuration with $\alpha = -5$, $\beta = -\frac{1}{2}$, $a_1 = 0$, $a_3 = 1$, and $a_5 = 60$. In panel (a) $\zeta_1 = \zeta_2 = 0$, and panels (b) and (c) $\zeta_1 = \frac{1}{30}$, $\zeta_2 = \frac{1}{5}$. The peaks are arranged in a rotated triangular pattern controlled by parameter phases.

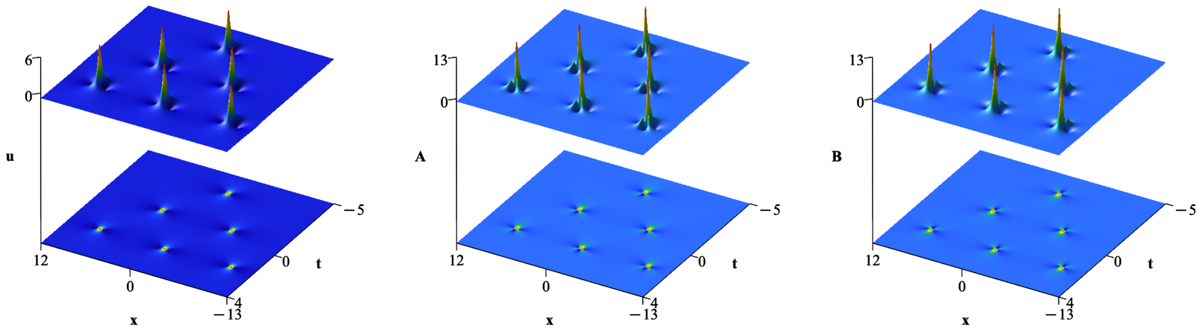

(a) **(b)** **(c)**

Figure 13. Third-order rogue wave exhibiting pentagonal configuration with parameters $\alpha = -5$, $\beta = -\frac{1}{2}$, $a_1 = 0$, $a_3 = 20$, and $a_5 = -1$. In panel (a) $\zeta_1 = \zeta_2 = 0$, and panels (b) and (c) $\zeta_1 = \frac{1}{30}$, $\zeta_2 = \frac{1}{5}$: Higher-order parameters generate polygonal rogue wave geometry while preserving peak amplitude.

It should be emphasized that the orientation and spatial rotation of the resulting rogue wave patterns, including triangular, pentagonal, heptagonal, and higher-order polygonal structures, are not fixed. Instead, they depend sensitively on the arguments (phases) of the complex parameters a_3, a_5, a_7, and higher-order terms. Variations in these arguments lead to rotations of the entire rogue wave configuration in the (x, t) plane, while preserving the overall geometric structure and peak amplitudes, as stated in Proposition 1. This behavior is also illustrated in Figure 9 and can be observed by comparing Figures 12 and 13. This behavior is closely related to the algebraic properties of the underlying tau-function and is believed to be connected to the root distributions of the Yablonskii–Vorob'ev polynomials [45] that arise in the construction of higher-order rogue wave solutions [46,47]. Although our numerical observations clearly indicate a strong correspondence between the rogue wave patterns and the associated polynomial root structures, a systematic analytical investigation of this relationship lies beyond the scope of the present work and is therefore left for future study.

By setting $\zeta_1 = \zeta_2 = 0$ in rogue wave solutions Eq (3.4), the resulting expressions coincide with those reported in [48] for the second-order BO equation. To date, no breather or semi-rational solutions have been obtained for the classical second-order BO equation. Our results show that, by taking $\zeta_1 = \zeta_2 = 0$, such solutions can be explicitly recovered. In the particular case when $\beta = -1$ and $2u_0\alpha = 1$, the bilinear form of the AB-BO equation reduces to that of the Boussinesq-type equation. In this scenario, taking $\zeta_1 = \zeta_2 = 0$ reproduces all the solutions previously reported in [49]. Moreover, by setting $\beta = -\frac{1}{3}$ and $2u_0\alpha = 1$, for arbitrary ζ_1 and ζ_2, the AB-BO Eq (1.6) reduces to the AB-Boussinesq equation [50]. This allows us to obtain breather, semi-rational, and rogue wave solutions for the AB-Boussinesq equation via the KP-reduction method, which have not been reported previously in the literature. These observations indicate that higher-dimensional systems which can be reduced to the (1+1)-dimensional bilinear form Eq (1.8) via symmetry or other reductions may also admit solutions of the type constructed in this work.

4. Concluding remarks

In this work, we have systematically investigated the nonlinear wave structures of the second-order AB-BO system. By employing the KP-hierarchy reduction method, we first constructed breather-type solutions in explicit Gram-determinant form and analyzed their dynamical behaviors. It was shown that different parameter selections lead to a rich variety of wave patterns, including fundamental and higher-order breathers as well as mixed breather-soliton interactions. The higher-order correction parameters ζ_1 and ζ_2 were demonstrated to play distinct physical roles: ζ_1 primarily induces spatial asymmetry and directional deformation, while ζ_2 governs spatiotemporal modulation and tilting effects.

Furthermore, by decomposing the determinant structure and applying long-wave limits, we derived semi-rational solutions describing interactions between lump (rogue wave) and breather or soliton components. These solutions reveal complex energy exchange mechanisms and hybrid localized structures that have no counterparts in purely local models. In addition, using Schur polynomial techniques and bilinear formalism, we obtained general higher-order rogue wave solutions in compact determinant form. The dynamical analysis showed that free complex parameters control the geometric arrangement and rotation of rogue wave peaks without altering their maximum amplitude. Depending on parameter choices, higher-order rogue waves exhibit triangular, pentagonal, and more general polygonal configurations, highlighting deep connections with the algebraic structure of the underlying tau-functions.

Overall, our results provide a unified determinant framework for constructing breather, semi-rational, and rogue wave solutions of the second-order AB-BO system. The findings significantly enrich the solution space of nonlocal integrable equations and contribute to a deeper understanding of correlated nonlinear wave phenomena in AB systems. Future work may focus on analytical investigations of the connection between rogue wave geometry and special polynomial root distributions, as well as potential physical applications of these nonlocal wave structures.

Author contributions

Majid Madadi: Software, visualization, writing-original draft, methodology, validation, conceptualization; Lanre Akinyemi: Software, visualization, writing-original draft, methodology, validation, conceptualization. All authors have read and approved the final version of the manuscript for publication

Use of Generative-AI tools declaration

The authors declare they have not used Artificial Intelligence (AI) tools in the creation of this article.

Conflict of interest

Prof. Lanre Akinyemi is the Guest Editor of special issue "Advances in Soliton Theory: New Perspectives and Applications" for AIMS Mathematics. Prof. Lanre Akinyemi was not involved in the editorial review and the decision to publish this article. The authors declare that they have no conflicts of interest.

References

1. J. Cohen, J. A. Screen, J. C. Furtado, M. Barlow, D. Whittleston, D. Coumou, et al., Recent Arctic amplification and extreme mid-latitude weather, *Nature Geosci.*, **7** (2014), 627–637. https://doi.org/10.1038/ngeo2234
2. J. A. Screen, Arctic amplification decreases temperature variance in northern mid-to high-latitudes, *Nature Clim. Change*, **4** (2014), 577–582. https://doi.org/10.1038/nclimate2268
3. J. M. Wallace, D. S. Gutzler, Teleconnections in the geopotential height field during the Northern Hemisphere winter, *Mon. Weather Rev.*, **109** (1981), 784–812.
4. B. P. Abbott, R. Abbott, T. D. Abbott, M. R. Abernathy, F. Acernese, K. Ackley, et al., Observation of gravitational waves from a binary black hole merger, *Phys. Rev. Lett.*, **116** (2016), 061102. https://doi.org/10.1103/PhysRevLett.116.061102
5. A. Aspect, P. Grangier, G. Roger, Experimental realization of Einstein-Podolsky-Rosen-Bohm Gedankenexperiment: A new violation of Bell's inequalities, *Phys. Rev. Lett.*, **49** (1982), 91. https://doi.org/10.1103/PhysRevLett.49.91
6. C. H. Bennett, G. Brassard, *Proceedings of the IEEE international conference on computers, systems and signal processing*, New York, 1984.
7. M. J. Ablowitz, Z. H. Musslimani, Integrable nonlocal nonlinear Schrödinger equation, *Phys. Rev. Lett.*, **110** (2013), 064105. https://doi.org/10.1103/PhysRevLett.110.064105
8. S. Y. Lou, F. Huang, Alice-Bob physics: coherent solutions of nonlocal KdV systems, *Sci. Rep.*, **7** (2017), 869. https://doi.org/10.1038/s41598-017-00844-y
9. C. C. Li, S. Y. Lou, M. Jia, Coherent structure of Alice-Bob modified Korteweg-de Vries equation, *Nonlinear Dyn.*, **93** (2018), 1799–1808. https://doi.org/10.1007/s11071-017-3895-1
10. W. B. Wu, S. Y. Lou, Exact solutions of an Alice-Bob KP equation, *Commun. Theor. Phys.*, **7** (2017), 629. https://doi.org/10.1088/0253-6102/71/6/629
11. S. Y. Lou, Alice-Bob systems, Ps-Td-C principles and multi-soliton solutions, 2016, arXiv:1603.03975.
12. S. Y. Lou, Alice-Bob systems, $\hat{P}$-$\hat{T}$-$\hat{C}$ symmetry invariant and symmetry breaking soliton solutions, *J. Math. Phys.*, **59** (2018), 083507. https://doi.org/10.1063/1.5051989
13. T. B. Benjamin, Internal waves of permanent form in fluids of great depth, *J. Fluid Mech.*, **29** (1967), 559–592. https://doi.org/10.1017/S002211206700103X
14. H. Ono, Algebraic solitary waves in stratified fluids, *J. Phys. Soc. Jpn.*, **39** (1975), 1082-1091. https://doi.org/10.1143/JPSJ.39.1082
15. A. S. Fokas, B. Fuchssteiner, The hierarchy of the Benjamin-Ono equation, *Phys. Lett. A*, **86** (1981), 341–345. https://doi.org/10.1016/0375-9601(81)90551-X
16. H. Leblond, D. Mihalache, Models of few optical cycle solitons beyond the slowly varying envelope approximation, *Phys. Rep.*, **523** (2013), 61–126. https://doi.org/10.1016/j.physrep.2012.10.006

17. W. Hereman, P. P. Banerjee, A. Korpel, G. Assanto, A. Van Immerzeele, A. Meerpoel, Exact solitary wave solutions of nonlinear evolution and wave equations using a direct algebraic method, *J. Phys. A: Math. Gen.*, **19** (1986), 607. https://doi.org/10.1088/0305-4470/19/5/016
18. A. Korpel, P. P. Banerjee, A heuristic guide to nonlinear dispersive wave equations and soliton-type solutions, *P. IEEE*, **72** (1984), 1109–1130. https://doi.org/10.1109/PROC.1984.12992
19. J. Boussinesq, Théorie de l'intumescence liquide appelée onde solitaire ou de translation se propageant dans un canal rectangulaire, *C. R. Acad. Sci. Paris*, **72** (1871), 755–759.
20. Y. Y. Li, H. C. Hu, Nonlocal symmetries and interaction solutions of the Benjamin-Ono equation, *Appl. Math. Lett.*, **75** (2018), 18–23. https://doi.org/10.1016/j.aml.2017.06.012
21. N. Taghizadeh, M. Mirzazadeh, F. Farahrooz, Exact soliton solutions for second-order Benjamin-Ono equation, *Appl. Appl. Math.*, **6** (2011), 31.
22. Y. S. Özkan, Double reduction of second order Benjamin-Ono equation via conservation laws and the exact solutions, *Balıkesir Üniversitesi Fen Bilimleri Enstitüsü Dergisi*, **23** (2021), 210–223.
23. G. L. He, L. He, The application of trigonal curve theory to the second-order Benjamin-Ono hierarchy, *Adv. Differ. Equ.*, **2014** (2014), 195. https://doi.org/10.1186/1687-1847-2014-195
24. W. Liu, High-order rogue waves of the Benjamin-Ono equation and the nonlocal nonlinear Schrödinger equation, *Mod. Phys. Lett. B*, **31** (2017), 1750269. https://doi.org/10.1142/S0217984917502694
25. W. Tan, Z. D. Dai, Spatiotemporal dynamics of lump solution to the (1+1)-dimensional Benjamin-Ono equation, *Nonlinear Dyn.*, **89** (2017), 2723–2728. https://doi.org/10.1007/s11071-017-3620-0
26. W. Shen, Z. Y. Ma, J. X. Fei, Q. Y. Zhu, J. C. Chen, Abundant symmetry-breaking solutions of the nonlocal Alice-Bob Benjamin-Ono system, *Complexity*, **2020** (2020), 2370970. https://doi.org/10.1155/2020/2370970
27. C. Gilson, F. Lambert, J. Nimmo, R. Willox, On the combinatorics of the Hirota D-operators, *Proc. A*, **452** (1996), 223–234. https://doi.org/10.1098/rspa.1996.0013
28. L. Akinyemi, Robustness of localized waves under temporal modulation in higher-dimensional nonlinear evolution equations, *Phys. Lett. A*, **576** (2026), 131411. https://doi.org/10.1016/j.physleta.2026.131411
29. M. Madadi, L. Akinyemi, K. Hosseini, Wronskian and rational solutions of a (2+1)-dimensional nonlinear evolution equation with time-dependent coefficients, *Nonlinear Dyn.*, **114** (2026), 274. https://doi.org/10.1007/s11071-025-12151-7
30. P. Chatterjee, L. Mandi, The separation of one-soliton-shock to multi-soliton-shock of dustion acoustic wave using Lax pair and Darboux transformation of Burgers'equation, *Phys. Fluids*, **35** (2023), 087131. https://doi.org/10.1063/5.0160542
31. F. J. Yu, L. Li, Soliton robustness, interaction and stability for a variable coefficients Schrödinger (VCNLS) equation with inverse scattering transformation, *Chaos Soliton. Fract.*, **185** (2024), 115185. https://doi.org/10.1016/j.chaos.2024.115185
32. M. Z. Raza, M. A. B. Iqbal, A. Khan, D. K. Almutairi, T. Abdeljawad, Soliton solutions of the (2+1)-dimensional Jaulent-Miodek evolution equation via effective analytical techniques, *Sci. Rep.*, **15** (2025), 3495. https://doi.org/10.1038/s41598-025-87785-z

33. L. Akinyemi, H. Rezazadeh, Q. H. Shi, M. Inc, M. M. Khater, H. Ahmad, et al., New optical solitons of perturbed nonlinear Schrödinger-Hirota equation with spatio-temporal dispersion, *Res. Phys.*, **29** (2021), 104656. https://doi.org/10.1016/j.rinp.2021.104656
34. M. Madadi, E. Asadi, Rogue waves from Kadomtsev-Petviashvili reduction: systematic derivation and dynamics in an extended Kadomtsev-Petviashvili equation, *J. Appl. Math. Comput.*, **72** (2026), 72. https://doi.org/10.1007/s12190-025-02733-4
35. E. Date, M. Jimbo, M. Kashiwara, T. Miwa, Transformation groups for soliton equations-Euclidean Lie algebras and reduction of the KP hierarchy, *Publ. Res. Inst. Math. Sci.*, **18** (1982), 1077–1110. https://doi.org/10.2977/prims/1195183297
36. M. Sato, Soliton equations as dynamical systems on infinite dimensional Grassmann manifold, *North-Holland Mathematics Studies*, **81** (1983), 259–271. https://doi.org/10.1016/S0304-0208(08)72096-6
37. R. Hirota, *The direct method in soliton theory*, Cambridge: Cambridge University Press, 2004. https://doi.org/10.1017/CBO9780511543043
38. W. Liu, A.-M. Wazwaz, X. X. Zheng, Families of semi-rational solutions to the Kadomtsev-Petviashvili I equation, *Commun. Nonlinear Sci.*, **67** (2019), 480–491. https://doi.org/10.1016/j.cnsns.2018.07.020
39. M. J. Ablowitz, J. Satsuma, Solitons and rational solutions of nonlinear evolution equations, *J. Math. Phys.*, **19** (1978), 2180–2186. https://doi.org/10.1063/1.523550
40. Y. Ohta, J. K. Yang, General high-order rogue waves and their dynamics in the nonlinear Schrödinger equation, *Proc. A*, **468** (2012), 1716–1740. https://doi.org/10.1098/rspa.2011.0640
41. B. Yang, J. K. Yang, General rogue waves in the Boussinesq equation, *J. Phys. Soc. Jpn.*, **89** (2020), 024003. https://doi.org/10.7566/JPSJ.89.024003
42. M. Madadi, M. Inc, Determinantal solutions to the (3+1)-dimensional Painlevé-type evolution equation; higher-order rogue and soliton waves, *Wave Motion*, **139** (2025), 103624. https://doi.org/10.1016/j.wavemoti.2025.103624
43. Y. K. Liu, B. Li, Dynamics of rogue waves on multisoliton background in the Benjamin-Ono equation, *Pramana*, **88** (2017), 57. https://doi.org/10.1007/s12043-016-1361-0
44. W. B. Ma, B. Sudao, H. B. Shao, Multiple rogue wave solutions of the (1+1)-dimensional Benjamin-Ono equation, *Phys. Scr.*, **99** (2024), 065219. https://doi.org/10.1088/1402-4896/ad40d9
45. P. A. Clarkson, E. L. Mansfield, The second Painlevé equation, its hierarchy and associated special polynomials, *Nonlinearity*, **16** (2003), R1. https://doi.org/10.1088/0951-7715/16/3/201
46. B. Yang, J. K. Yang, Rogue wave patterns in the nonlinear Schrödinger equation, *Physica D*, **419** (2021), 132850. https://doi.org/10.1016/j.physd.2021.132850
47. P. Huang, Y. K. Wang, D. Zhou, Rogue wave patterns of Newell type long-wave-short-wave model, *Chaos Soliton. Fract.*, **175** (2023), 114038. https://doi.org/10.1016/j.chaos.2023.114038
48. F. Z. Zheng, Z. Y. Qin, G. Mu, T. Y. Wang, On the Role of AM Polynomial Roots in the Determination of Rogue Wave Patterns in Benjamin-ono Equation, *Nonlinear Dyn.*, **113** (2025), 21703–21723. https://doi.org/10.1007/s11071-025-11273-2

49. L. K. Yunkai, L. Biao, A.-M. Wazwaz, Novel high-order breathers and rogue waves in the Boussinesq equation via determinants, *Math. Meth. Appl. Sci.*, **43** (2020), 3701–3715. https://doi.org/10.1002/mma.6148
50. P. Dong, Z.-Y. Ma, J.-X. Fei, W.-P. Cao, The shifted parity and delayed time-reversal symmetry-breaking solutions for the (1+1)-dimensional Alice–Bob Boussinesq equation, *Front. Phys.*, **11** (2023), 1137999. https://doi.org/10.3389/fphy.2023.1137999